

A Wavelet-Enhanced PWT-D-Accelerated Time-Domain Integral Equation Solver for Analysis of Transient Scattering from Electrically Large Conducting Objects

Yang Liu, *Member, IEEE*, Abdulkadir C. Yücel, Hakan Bağcı, *Senior Member, IEEE*, Anna C. Gilbert, Eric Michielssen, *Fellow, IEEE*

Abstract—A wavelet-enhanced plane-wave time-domain (PWT-D) algorithm for efficiently and accurately solving time-domain surface integral equations (TD-SIEs) on electrically large conducting objects is presented. The proposed scheme reduces the memory requirement and computational cost of the PWT-D algorithm by representing the PWT-D ray data using local cosine wavelet bases (LCBs) and performing PWT-D operations in the wavelet domain. The memory requirement and computational cost of the LCB-enhanced PWT-D-accelerated TD-SIE solver, when applied to the analysis of transient scattering from smooth quasi-planar objects with near-normal incident pulses, scale nearly as $O(N_s \log N_s)$ and $O(N_s^{1.5})$, respectively. Here, N_s denotes the number of spatial unknowns. The efficiency and accuracy of the proposed scheme are demonstrated through its applications to the analysis of transient scattering from a 185 wavelength-long NASA almond and a 123-wavelength long Airbus-A320 model.

Index Terms—Fast algorithms, marching-on-in-time (MOT), wavelet, local cosine basis (LCB), plane-wave time-domain algorithm (PWT-D), time-domain surface integral equation (TD-SIE), transient scattering, very large-scale problems, complexity analysis.

I. INTRODUCTION

Multilevel plane-wave time-domain (PWT-D)-accelerated and marching-on-in-time (MOT)-based time-domain (TD) surface integral equation (SIE) solvers represent an intriguing alternative to finite-difference time-domain solvers for

Manuscript received xx xx, xxxx. This work was supported in part by the AFOSR/NSSFF Program under Award FA9550-10-1-0180 and the National Science Foundation (NSF) under Grant CCF 1116082.

Y. Liu, A. C. Yücel and E. Michielssen are with the Department of Electrical Engineering and Computer Science, University of Michigan, Ann Arbor, MI 48109, USA (e-mails: liuyangz@umich.edu, acyucel@umich.edu, emichiel@umich.edu).

H. Bağcı is with the Division of Computer, Electrical, and Mathematical Sciences and Engineering (CEMSE), King Abdullah University of Science and Technology (KAUST), Thuwal 23955, Saudi Arabia, (e-mail: hakan.bagci@kaust.edu.sa).

A. C. Gilbert is with the Department of Mathematics, University of Michigan, Ann Arbor, MI 48109, USA (e-mail: annacg@umich.edu).

analyzing transient scattering from large and complex, perfect electrically conducting (PEC) [1] or homogenous penetrable [2] objects. PWT-D-TD-SIE solvers are the time-domain counterparts of multilevel fast multipole (MLFMA)-accelerated frequency domain (FD) integral equation solvers [3]. Their memory requirement and computational cost scale as $O(N_s^{1.5})$ and $O(N_s N_s \log^2 N_s)$ respectively. Here, N_s is the number of spatial unknowns and $N_t \propto O(N_s^{0.5})$ is the number of time steps.

Despite their reduced memory requirement and computational cost, for many years the usefulness of PWT-D-TD-SIE solvers suffered from a lack of efficient PWT-D parallelization schemes. Recently, provably scalable parallelization strategies, which hierarchically partition the inherently heterogeneous PWT-D workload, have been developed; these methods have enabled TD-SIE solvers to efficiently solve transient scattering problems involving in excess of 10 million spatial unknowns [4]. Unfortunately, even when benefitting from parallel implementations, the memory requirement of PWT-D-TD-SIE solvers oftentimes remains one order of magnitude larger than that of their MLFMA-FD-SIE counterparts, this mainly because of the need to store temporal PWT-D ray data.

In this work, a wavelet compression scheme is developed to reduce the memory requirement of parallel PWT-D-TD-SIE solvers. Previously, wavelets (and related wavelet packets) have been used to accelerate the solution of both FD-SIEs [5–9] and TD-SIEs [10, 11], principally by using wavelet representations of surface currents to enable sparsification of interaction matrices. In this work, in contrast, wavelets are used to exploit the temporal sparsity of PWT-D ray data that encodes the temporal far-field plane wave signatures of oct-tree arranged sources. This use of wavelets to compress PWT-D ray data is motivated by two observations. (i) PWT-D-TD-SIE solvers, much like their MLFMA-FD-SIE counterparts, use vastly different schemes to evaluate “near” and “far” field source-observer interactions. Near-field interactions are localized in both space and time and accounted for classically. Far-field interactions are nonlocal in both space and time and evaluated using plane wave bases. The memory requirement

and computational cost associated with the evaluation of far-field interactions dwarf those of near-field ones. Hence, algorithmic improvements aimed at reducing the memory requirement and computational cost of PWT-D-TD-SIE solvers should target compression of PWT-D plane wave / ray data as opposed to that of current representations. (ii) Transient scattering problems often involve objects that are illuminated by short-duration and high-frequency temporal pulses. These pulses induce spatially and temporally localized surface current densities, which in turn generate PWT-D ray data with similar qualities.

We therefore develop a wavelet-enhanced implementation of the PWT-D algorithm, which represents PWT-D ray data using local cosine wavelet bases (LCBs) [12] and performs most PWT-D operations directly in the wavelet domain. LCBs are chosen over other wavelets due to their effectiveness in representing high frequency signals and integral kernels [9, 13]. The proposed LCB-enhanced PWT-D algorithm significantly reduces the memory requirement *and* computational cost of the conventional PWT-D algorithm. The scheme is incorporated into a TD-SIE solver to enable efficient and accurate analysis of transient scattering from electrically large PEC objects. The capabilities of the solver are demonstrated via its application to scattering problems involving canonical and real-world objects spanning well over a hundred wavelengths.

II. MOT-BASED SOLUTION OF TD-SIES AND ITS PWT-D ACCELERATION

A. TD-SIES and MOT Scheme

Let S denote the closed surface of a PEC scatterer that resides in free space. An incident electromagnetic field $\{\mathbf{E}^i(\mathbf{r}, t), \mathbf{H}^i(\mathbf{r}, t)\}$, assumed temporally bandlimited with maximum angular frequency ω_{max} and vanishingly small for $t < 0$, excites S . The current density $\mathbf{J}(\mathbf{r}, t)$ induced on S in response to this excitation generates a scattered field. The total field $\{\mathbf{E}(\mathbf{r}, t), \mathbf{H}(\mathbf{r}, t)\}$, which is obtained by adding the scattered field to the incident field, satisfies the boundary conditions $\hat{\mathbf{n}} \times \hat{\mathbf{n}} \times \partial_t \mathbf{E}(\mathbf{r}, t) = 0$ and $\hat{\mathbf{n}} \times \partial_t \mathbf{H}(\mathbf{r}, t) = 0$, $\forall \mathbf{r} \in S^-$. Here, $\hat{\mathbf{n}}$ denotes the outward pointing unit normal to S , ∂_t represents the time derivative, and S^- denotes the surface conformal to, but just inside, S . Enforcement of these boundary conditions yields time-domain electric and magnetic field integral equations (TD-EFIE and TD-MFIE)

$$\hat{\mathbf{n}} \times \hat{\mathbf{n}} \times \partial_t \mathbf{E}^i(\mathbf{r}, t) = \mathcal{L}_e[\mathbf{J}](\mathbf{r}, t) \quad (1)$$

$$\hat{\mathbf{n}} \times \partial_t \mathbf{H}^i(\mathbf{r}, t) = \mathcal{L}_h[\mathbf{J}](\mathbf{r}, t) \quad (2)$$

$\forall \mathbf{r} \in S^-$. In (1)-(2) the TD-EFIE and TD-MFIE operators \mathcal{L}_e and \mathcal{L}_h

$$\mathcal{L}_e[\mathbf{J}](\mathbf{r}, t) = \hat{\mathbf{n}} \times \hat{\mathbf{n}} \times \frac{\mu_0}{4\pi} \int_S dS' (\partial_t^2 \mathcal{I} - c_0^2 \nabla \nabla) \cdot \frac{\mathbf{J}(\mathbf{r}', \tau)}{R} \quad (3)$$

$$\begin{aligned} \mathcal{L}_h[\mathbf{J}](\mathbf{r}, t) = & \frac{1}{4\pi} \hat{\mathbf{n}} \times \int_S dS' (\mathbf{r} - \mathbf{r}') \times \\ & [\frac{1}{c_0 R^2} \partial_t^2 \mathbf{J}(\mathbf{r}', \tau) + \frac{1}{R^3} \partial_t \mathbf{J}(\mathbf{r}', \tau)]. \end{aligned} \quad (4)$$

Here, \mathcal{I} is the identity operator, $R = |\mathbf{r} - \mathbf{r}'|$ is the distance between source point \mathbf{r}' and observation point \mathbf{r} , $\tau = t - R/c_0$ represents retarded time, and $c_0 = 1/\sqrt{\epsilon_0 \mu_0}$, ϵ_0 , and μ_0 denote the speed of light, permittivity, and permeability in free space, respectively. The TD-EFIE and TD-MFIE, however, are plagued by interior resonances because of the presence of the operators' null space for oscillating currents [14, 15]. The time-domain combined field integral equation (TD-CFIE) linearly combines TD-EFIE (1) and TD-MFIE (2) as

$$\hat{\mathbf{n}} \times \partial_t \mathbf{H}^i(\mathbf{r}, t) - \beta/\eta_0 \hat{\mathbf{n}} \times \hat{\mathbf{n}} \times \partial_t \mathbf{E}^i(\mathbf{r}, t) = \mathcal{L}_c[\mathbf{J}](\mathbf{r}, t) \quad (5)$$

where $\mathcal{L}_c[\mathbf{J}](\mathbf{r}, t) = \mathcal{L}_h[\mathbf{J}](\mathbf{r}, t) - \beta/\eta_0 \mathcal{L}_e[\mathbf{J}](\mathbf{r}, t)$, β is a combination constant, and $\eta_0 = \sqrt{\mu_0/\epsilon_0}$ is the free-space intrinsic impedance. Contrary to the TD-EFIE and TD-MFIE, TD-CFIE does not support any resonant modes.

To numerically solve (5), $\mathbf{J}(\mathbf{r}, t)$ is expanded in terms of spatial basis functions $\mathbf{S}_n(\mathbf{r})$, $n = 1, \dots, N_s$, and temporal basis functions $T_i(t)$, $i = 1, \dots, N_t$, as

$$\mathbf{J}(\mathbf{r}, t) = \sum_{n=1}^{N_s} \mathbf{S}_n(\mathbf{r}) f_n(t) = \sum_{n=1}^{N_s} \sum_{i=1}^{N_t} I_{n,i} \mathbf{S}_n(\mathbf{r}) T_i(t). \quad (6)$$

Here, $f_n(t)$ is the temporal signature of the n^{th} spatial basis function $\mathbf{S}_n(\mathbf{r})$, and $I_{n,i}$ is the unknown coefficient of the space-time basis function $\mathbf{S}_n(\mathbf{r}) T_i(t)$. The i^{th} temporal basis function $T_i(t) = T(t - i\Delta t)$ is nonzero for $t \geq (i-1)\Delta t$; here $\Delta t = \pi/(\chi \omega_{max})$ is the time step size and $\chi > 1$ is a temporal oversampling factor. In this study, spatial and temporal basis functions $\mathbf{S}_n(\mathbf{r})$ and $T(t)$ are chosen to be Rao-Wilton-Glisson functions [16] and fourth order Lagrange polynomials [17], respectively. Substituting (6) into (5) and (Galerkin) testing the resulting equation with spatial basis functions $\mathbf{S}_m(\mathbf{r})$, $m = 1, \dots, N_s$, at times $t = j\Delta t$, $j = 1, \dots, N_t$, yields the N_t linear systems

$$\bar{\bar{\mathbf{Z}}}_0 \bar{\mathbf{I}}_j = \bar{\mathbf{F}}_j - \sum_{i=1}^{j-1} \bar{\bar{\mathbf{Z}}}_i \bar{\mathbf{I}}_{j-i} \quad (7)$$

where $\{\bar{\mathbf{I}}_j\}_n = I_{\underline{n}, j}$, $n = 1, \dots, N_s$ and the entries of the vector $\bar{\mathbf{F}}_j$ and matrix $\bar{\bar{\mathbf{Z}}}_j$

$$\{\bar{\mathbf{F}}_j\}_m = \langle \mathbf{S}_m(\mathbf{r}), \hat{\mathbf{n}} \times \partial_t \mathbf{H}^i(\mathbf{r}, t) - \beta/\eta_0 \hat{\mathbf{n}} \times \hat{\mathbf{n}} \times \partial_t \mathbf{E}^i(\mathbf{r}, t) \rangle \Big|_{t=j\Delta t} \quad (8)$$

$$\{\bar{\bar{\mathbf{Z}}}_j\}_{mn} = \langle \mathbf{S}_m(\mathbf{r}), \mathcal{L}_c[\mathbf{S}_n T](\mathbf{r}, t) \rangle \Big|_{t=j\Delta t}. \quad (9)$$

Here, both $m, n = 1, \dots, N_s$, and $\langle \cdot, \cdot \rangle$ denotes the standard inner product. The coefficient vectors $\bar{\mathbf{I}}_j$, $j = 1, \dots, N_t$ can be solved for recursively, by MOT: After $\bar{\mathbf{I}}_j$ is obtained by solving the matrix system (7) at time step j , it is used along with $\bar{\mathbf{I}}_i$, $i = 1, \dots, j-1$, which are solved for at prior time steps, to

compute the sum on the right hand side (RHS) of (7) at time step $j+1$. Computation of these sums for all time steps represents a major computational bottleneck, and requires $O(N_t N_s^2)$ operations and $O(N_s^2)$ memory. Consequently, the memory requirement and computational cost of classical MOT schemes are prohibitively high when applied to the analysis of scattering from electrically large PEC structures.

B. The Multilevel PWTD Algorithm

The multilevel PWTD algorithm permits the fast computation of the RHS of (7) in $O(N_t N_s \log^2 N_s)$ operations, requiring only $O(N_s^{1.5})$ memory. In this section, the conventional (as opposed to LCB-enhanced) multilevel PWTD algorithm is briefly summarized to introduce the notation and emphasize details that are pertinent to the description of the proposed LCB-enhanced PWTD algorithm that follows. Other details of the conventional multilevel PWTD algorithm's description can be found in [1, 2, 18].

Consider a rectangular box that encloses S and is recursively subdivided into eight boxes until the linear dimensions of the smallest boxes thus obtained are proportional to the wavelength at the maximum frequency, $\lambda = 2\pi c_0 / \omega_{max}$. This recursive subdivision gives rise to an N_L -level PWTD tree with levels $v = 1, \dots, N_L = O(\log(N_s^{0.5}))$. The tree's finest level ($v=1$) contains the smallest boxes while its coarsest level ($v=N_L$) is the box enclosing S . Let N_g^v denote the number of nonempty boxes at level v . For surface scatterers, $N_g^1 = O(N_s)$ and $N_g^{v+1} \approx N_g^v / 4$. The radius of a sphere enclosing a level- v box is $R^v = 2^{(v-1)} R^1$ with $R^1 = O(1)$.

Upon constructing the PWTD tree, far-field box pairs are identified for each level starting with level $N_L - 2$. Two same-level nonempty boxes are labeled a “level- v far-field box pair” if the distance between their centers is greater than γR^v ($3 < \gamma < 6$) and their respective parent boxes do not constitute a far-field pair. Two finest level nonempty boxes that do not constitute a far-field pair constitute a near-field pair; each nonempty finest level box also forms a near-field pair with itself. Interactions between spatial basis functions residing in near-field box pairs are computed directly using (9) and their contributions added to the RHS of (7). Interactions between spatial basis functions contained in far-field box pairs are evaluated by the PWTD scheme.

Let α and α' denote a far-field box pair's source and observer boxes, respectively. Let \mathbf{r}_s^c and \mathbf{r}_o^c denote these boxes' centers and let $R_{c,\alpha\alpha'} = |\mathbf{r}_{c,\alpha\alpha'}| = |\mathbf{r}_o^c - \mathbf{r}_s^c|$. The source and observer boxes contain spatial basis functions $\mathbf{S}_n(\mathbf{r})$, $\forall n \in \alpha$, and $\mathbf{S}_m(\mathbf{r})$, $\forall m \in \alpha'$, respectively. For all $n \in \alpha$, the temporal signature $f_n(t)$ associated with $\mathbf{S}_n(\mathbf{r})$ is broken into N_l^v consecutive subsignals using a local approximate prolate spheroidal (APS) function $T^{APS}(t)$ [19] that is bandlimited to $\omega_s = \chi_t \omega_{max}$ and approximately time-limited to

$-p_f \Delta t < t < p_f \Delta t$, $5 \leq p_f \leq 10$, as

$$f_n(t) = \sum_{l=1}^{N_l^v} f_n^l(t) = \sum_{l=1}^{N_l^v} \sum_{j=(l-1)M^v+1}^{lM^v} I_{n,j} T_j^{APS}(t) \quad (10)$$

where $T_j^{APS}(t) = T^{APS}(t - j\Delta t)$ and $N_l M^v = N_t$; M^v is chosen such that the duration of each subsignal, $T^v = (M^v + 2p_f)\Delta t$, is less than $(R_{c,\alpha\alpha'} - 2R^v)/c_0$. Let $\mathbf{J}_\alpha^l(\mathbf{r}, t) = \sum_{n \in \alpha} \mathbf{S}_n(\mathbf{r}) f_n^l(t)$ denote the current due to the l^{th} subsignal associated with all source basis functions in box α . Fields produced by $\mathbf{J}_\alpha^l(\mathbf{r}, t)$ (and tested by $\mathbf{S}_m(\mathbf{r})$ in box α') can be computed as follows. (i) Construct a set of outgoing rays (of box α) in direction $\hat{\mathbf{k}}_{qp}^v$ by convolving the projection function $\mathbf{P}_n^+(\hat{\mathbf{k}}_{qp}^v, t, \hat{\mathbf{k}}_{qp}^v)$ with subsignal $f_n^l(t)$ as

$$\mathbf{G}_{l,\alpha}^+(\hat{\mathbf{k}}_{qp}^v, t) = \frac{\partial_t^2}{16\pi^2 c_0^2} \sum_{n \in \alpha} \mathbf{P}_n^+(\hat{\mathbf{k}}_{qp}^v, t, \hat{\mathbf{k}}_{qp}^v) * f_n^l(t) \quad (11)$$

where $*$ denotes temporal convolution, $t \in [t_l^{+s}, t_l^{+e}]$ with starting point $t_l^{+s} = ((l-1)M^v - p_f)\Delta t - R^v/c_0$ and ending point $t_l^{+e} = (lM^v + p_f)\Delta t + R^v/c_0$. (ii) Translate the outgoing rays (of box α) onto incoming rays (of box α') by convolving outgoing rays $\mathbf{G}_{l,\alpha}^+(\hat{\mathbf{k}}_{qp}^v, t)$ with the translation function $\mathcal{T}(\hat{\mathbf{k}}_{qp}^v, t)$ as

$$\mathbf{G}_{l,\alpha'}^-(\hat{\mathbf{k}}_{qp}^v, t) = \mathcal{T}(\hat{\mathbf{k}}_{qp}^v, t) * \mathbf{G}_{l,\alpha}^+(\hat{\mathbf{k}}_{qp}^v, t). \quad (12)$$

Here, $t \in [t_l^{-s}, t_l^{-e}]$ with the starting point $t_l^{-s} = ((l-1)M^v - p_f)\Delta t - (R^v + R_{c,\alpha\alpha'})/c_0$ and the ending point $t_l^{-e} = (lM^v + p_f)\Delta t + (R^v + R_{c,\alpha\alpha'})/c_0$. (iii) Project the incoming rays onto test functions $\mathbf{S}_m(\mathbf{r})$ in box α' by convolving the projection functions $\mathbf{P}_m^-(\hat{\mathbf{k}}_{qp}^v, t, \hat{\mathbf{k}}_{qp}^v)$ and $\mathbf{P}_m^-(\hat{\mathbf{k}}_{qp}^v, t, \hat{\mathbf{n}})$ with the incoming rays $\mathbf{G}_{l,\alpha'}^-(\hat{\mathbf{k}}_{qp}^v, t)$ and summing over all directions with quadrature weights ω_{qp}^v as

$$\left\langle \mathbf{S}_m(\mathbf{r}), \mathcal{L}_c[\mathbf{J}_\alpha^l](\mathbf{r}, t) \right\rangle = \sum_{q=0}^{K^v} \sum_{p=-K^v}^{K^v} \omega_{qp}^v \\ [-\beta \mathbf{P}_m^-(\hat{\mathbf{k}}_{qp}^v, t, \hat{\mathbf{k}}_{qp}^v) + \mathbf{P}_m^-(\hat{\mathbf{k}}_{qp}^v, t, \hat{\mathbf{n}})]^\dagger * \mathbf{G}_{l,\alpha'}^-(\hat{\mathbf{k}}_{qp}^v, t) \quad (13)$$

where the superscript \dagger denotes transpose, the number of ray directions $N_k^v = (K^v + 1)(2K^v + 1)$ with $K^v = \lfloor 2\chi_s \omega_s R^v / c_0 \rfloor + 1$, and χ_s is a spherical oversampling factor. In (11)-(13), the projection function

$$\mathbf{P}_{\{m,n\}}^\pm(\hat{\mathbf{k}}_{qp}^v, t, \hat{\mathbf{v}}) = \int_{S_{\{m,n\}}} dS' \hat{\mathbf{v}} \times \mathbf{S}_{\{m,n\}}(\mathbf{r}') \delta(t \pm \hat{\mathbf{k}}_{qp}^v \cdot (\mathbf{r}' - \mathbf{r}_{\{o,s\}}^c) / c_0) \quad (14)$$

where $S_{\{m,n\}}$ represents the support of $\mathbf{S}_{\{m,n\}}(\mathbf{r})$ and $\delta(\cdot)$ is the Dirac delta function. The translation function

$$\mathcal{T}(\hat{\mathbf{k}}_{qp}^v, t) = \frac{c_0 \partial_t}{R_{c,\alpha\alpha'}} \sum_{k=0}^{K^v} (2k+1) \Phi_k \left(\frac{c_0 t}{R_{c,\alpha\alpha'}} \right) \Phi_k(\cos \theta) \quad (15)$$

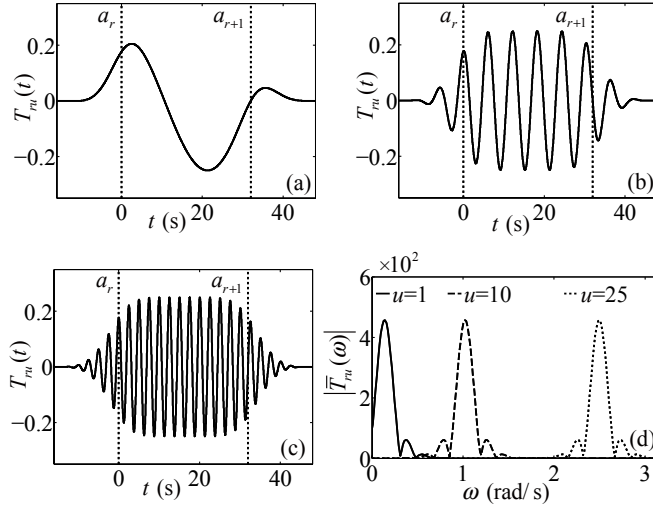


Fig. 1. The LCB functions $T_{ru}(t)$ associated with interval $[a_r, a_{r+1}]$, $a_r = 0$, $\Delta t = 1$ s, $N_u^r = 32$, $\varepsilon = 16$ with different central frequencies: (a) $u = 1$, (b) $u = 10$, (c) $u = 25$. (d) The Fourier transform $\bar{T}_{ru}(\omega)$ of (a), (b) and (c).

where $\Phi_k(\cdot)$ is the Legendre polynomial of degree k , $\cos \theta = \hat{\mathbf{k}}_{qp}^v \cdot \mathbf{R}_{c,\alpha\alpha'} / R_{c,\alpha\alpha'}$ and $|t| \leq R_{c,\alpha\alpha'} / c_0$. In practice, only outgoing/incoming rays of finest level boxes are constructed/projected directly from/onto spatial basis functions using (11)/(13); those of higher level boxes are computed via the global vector spherical interpolation/filtering [1, 20]. The computational complexity analyses in [18] concluded that the computational cost and memory requirement of the multilevel PWT-D accelerated MOT scheme scale as $O(N_t N_s \log^2 N_s)$ and $O(N_s^{1.5})$ for surface scatterers, respectively. Note: in the remainder of this paper, the computational cost of the conventional PWT-D-TD-SIE solver is rewritten as $O(N_s^{1.5} \log^2 N_s)$, since $N_t \propto O(N_s^{0.5})$ for electrically large nonresonant scatterers. In what follows, a scheme that further reduces the memory requirement and computational cost of conventional PWT-D algorithm by using LCBs to represent and manipulate ray data is proposed.

III. LCB-ENHANCED MULTILEVEL PWT-D ALGORITHM

A. Representation of the Ray Data Using LCBs

To represent a PWT-D ray data in terms of LCBs, the ray's temporal support $[t_l^{\pm s}, t_l^{\pm e}]$ is first partitioned into N intervals using a monotonically increasing sequence of numbers (a_r) , $r = 1, \dots, N$ with $a_1 = t_l^s - \varepsilon$, $a_N = t_l^e + \varepsilon$, and $0 < \varepsilon \leq (a_{r+1} - a_r) / 2$ for $\forall r < N$ [Note: here and in what follows, the symbol \pm in the superscripts of $t_l^{\pm s}$ and $t_l^{\pm e}$ is dropped]. It is assumed that the length of the r^{th} interval is an integer multiple of Δt , i.e., $a_{r+1} - a_r = M^r \Delta t$. On the r^{th} interval, the LCB functions $T_{ru}(t)$, $u \in \mathbb{N}$ are

$$T_{ru}(t) = B_r(t) \sqrt{\frac{2}{M^r \Delta t}} \cos \left((2u-1) \frac{t-a_r}{2M^r \Delta t} \pi \right) \quad (16)$$

where $B_r(t)$ is a smooth and compactly supported bell func-

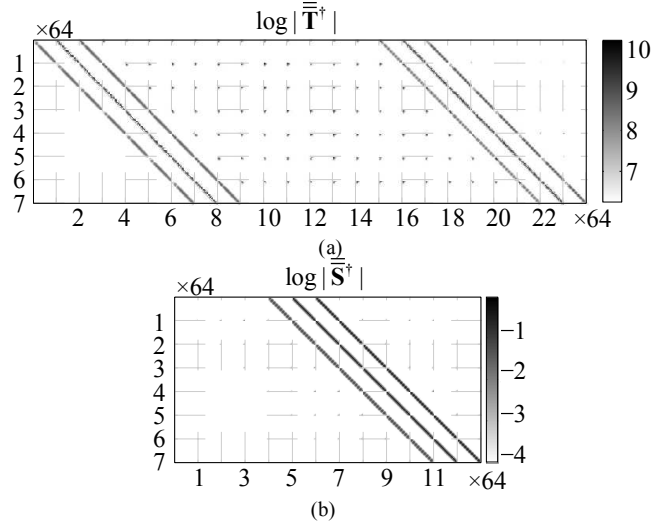


Fig. 2. (a) Magnitudes of a translation matrix $\bar{\mathbf{T}}^\dagger$ obtained by setting $\chi_t = 10$, $R^v = 3.5\lambda$, $\mathbf{R}_{c,\alpha\alpha'} = [24\lambda \ 0 \ 0]^{\dagger}$, $\hat{\mathbf{k}}_{qp}^v = [0 \ 0 \ 1]^{\dagger}$, $M^{\min} = 64$, $N^+ = 7$, and $N^- = 24$. (b) Magnitudes of a shifting matrix $\bar{\mathbf{S}}^\dagger$ obtained by setting $\chi_t = 10$, $R^v = 7\lambda$, $R^{v-1} = 3.5\lambda$, $\mathbf{R}_{c,\alpha\alpha'} = [4\lambda \ 4\lambda \ 4\lambda]^{\dagger}$, $\hat{\mathbf{k}}_{qp}^v = [1/\sqrt{3} \ 1/\sqrt{3} \ 1/\sqrt{3}]^{\dagger}$, $M^{\min} = 64$, $N^+ = 7$, and $N^{v-1} = 13$. The accuracy is set to 1×10^{-4} .

tion defined as

$$B_r(t) = \begin{cases} b\left(\frac{t-a_r}{\varepsilon}\right) & a_r - \varepsilon \leq t < a_r + \varepsilon \\ 1 & a_r + \varepsilon \leq t < a_{r+1} - \varepsilon \\ b\left(\frac{a_{r+1}-t}{\varepsilon}\right) & a_{r+1} - \varepsilon \leq t < a_{r+1} + \varepsilon \end{cases} \quad (17)$$

Here, the “cutoff function” $b(t)$ is chosen as [21]

$$b(t) = \sin \left(\frac{\pi}{4} + \frac{\pi}{4} \sin \left(\frac{\pi}{2} \sin \frac{\pi t}{2} \right) \right), \quad -1 \leq t \leq 1. \quad (18)$$

With the bell and cutoff functions in (17) and (18), the LCB functions $T_{ru}(t)$ are locally supported on the interval $[a_r - \varepsilon, a_{r+1} + \varepsilon]$ and orthonormal, i.e., $\langle T_{ru}(t), T_{sw}(t) \rangle = \delta_{rs} \delta_{uw}$, $\forall r, s < N$, $\forall u, w \in \mathbb{N}$, where δ_{rs} and δ_{uw} are Kronecker delta functions. Furthermore, the LCB functions are localized in frequency. Specifically, their Fourier transforms $\bar{T}_{ru}(\omega)$

$$\bar{T}_{ru}(\omega) = \sqrt{\frac{1}{2M^r \Delta t}} (e^{-ia_r \omega_u} \bar{B}_r(\omega - \omega_u) + e^{ia_r \omega_u} \bar{B}_r(\omega + \omega_u)) \quad (19)$$

where $\omega_u = \pi(u-1/2) / (M^r \Delta t)$ is the center frequency of $\bar{T}_{ru}(\omega)$ and $\bar{B}_r(\omega)$ is the Fourier transform of the bell function $B_r(t)$. The quasi-bandlimited nature of the LCB follows from the quasi-bandlimited nature of the bell function. To illustrate the above properties, LCB functions on a fixed interval with three different central frequencies are plotted in Figs. 1(a)-(c). Clearly, these functions are localized in time and frequency.

Next, the outgoing/incoming rays are represented using the LCBs defined by (16). The outgoing/incoming rays of a level- v

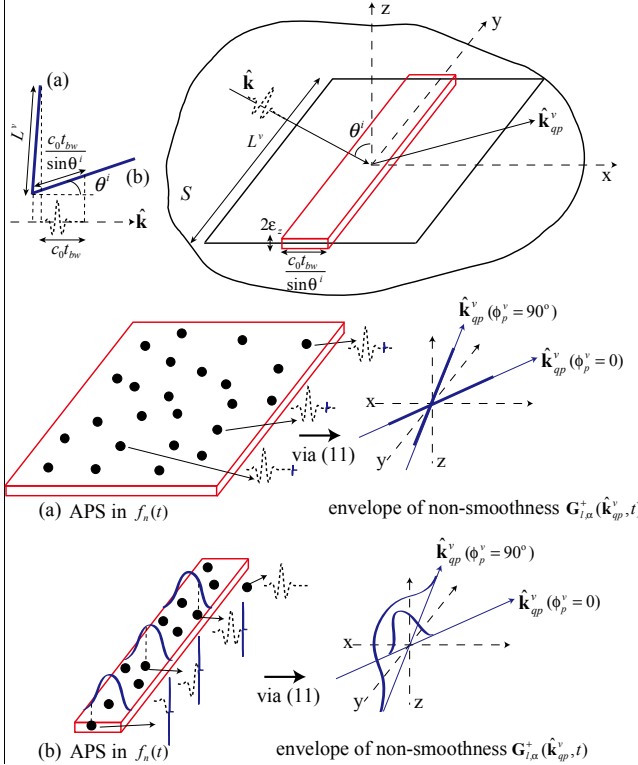


Fig. 3. Non-smoothness in $f_n(t)$ and envelope of non-smooth components of the outgoing rays (shown in solid blue lines) from one box with (a) near-normal and (b) grazing incidence of a modulated Gaussian pulse.

box in direction $\hat{\mathbf{k}}_q^v$ consist of two transverse components, i.e., $\mathbf{G}_{l,\alpha}^\pm(\hat{\mathbf{k}}_q^v, t) = G_\theta(\hat{\mathbf{k}}_q^v, t)\hat{\theta} + G_\phi(\hat{\mathbf{k}}_q^v, t)\hat{\phi}$, each of which is expressed using LCBs as

$$G_\psi(\hat{\mathbf{k}}_q^v, t) = \sum_{r=1}^N \sum_{u=1}^\infty I_{ru}^\psi(\hat{\mathbf{k}}_q^v) T_{ru}(t). \quad (20)$$

Here, $\psi = \{\theta, \phi\}$ and the LCB coefficients are expressed since $I_{ru}^\psi(\hat{\mathbf{k}}_q^v) = \langle G_\psi(\hat{\mathbf{k}}_q^v, t), T_{ru}(t) \rangle$ due to the orthonormality of the LCB functions. In practice, these coefficients are efficiently computed by first sampling the outgoing/incoming rays with time step size Δt and then applying a discrete local cosine transform (LCT), requiring $O(M' \log M')$ operations for each interval [21]. The LCT results in a coefficient vector

$$\bar{\mathbf{I}}_\psi(\hat{\mathbf{k}}_q^v) = [I_{11}^\psi(\hat{\mathbf{k}}_q^v), \dots, I_{1M'}^\psi(\hat{\mathbf{k}}_q^v), \dots, I_{N1}^\psi(\hat{\mathbf{k}}_q^v), \dots, I_{NM'}^\psi(\hat{\mathbf{k}}_q^v)]^\dagger. \quad (21)$$

Note that the number of LCB coefficients associated with the r^{th} interval is M' and the total number of LCB coefficients is $N_I = \sum_{r=1}^N M'$. With a proper choice of the partition sequence (a_r) , the coefficient vector $\bar{\mathbf{I}}_\psi(\hat{\mathbf{k}}_q^v)$ is numerically sparse on each interval [22] and only those coefficients with magnitudes exceeding a prescribed threshold need to be stored. Exploiting temporal features present in ray data encountered in the analysis of large scale scattering problems, two types of partitioning schemes are considered.

- *Single-resolution* bases partition the support of ray data using small intervals of equal length, i.e., $M' = M^{\min}, \forall r$,

and compute the LCB coefficients in $O(N_I \log M^{\min})$ operations.

- *Multi-resolution* bases combine adjacent intervals of the single-resolution bases that (i) have similar maximum LCB coefficients and (ii) exhibit rapidly decaying coefficients into larger intervals; they also compute the LCB coefficients on these new intervals using at most $O(N_I \log M^{\max})$ operations where $M^{\max} \Delta t$ is the maximum allowed interval length. In comparison, the conventional method to find partitions that yield maximum sparsity require $O(N_I \log^2 N_I)$ operations [21].

Note that in our implementation, the minimum and maximum interval lengths are chosen as constants, e.g., $M^{\min} = 16$ and $M^{\max} = 256$, hence computing the LCB coefficients with single- or multi-resolution bases requires $O(N_I)$ operations.

In general, multi-resolution bases achieve better sparsity in LCB coefficients than their single-resolution counterparts. That said, these bases (i.e., the optimal partitions) vary for each outgoing/incoming ray, which poses challenges when implementing PWTD operations directly in the wavelet domain. Therefore, the proposed LCB-enhanced PWTD scheme implements a hybrid strategy: the computation of the outgoing/incoming rays is carried out directly in the wavelet domain using single-resolution bases. Once computed, the ray data is stored using LCB coefficients derived from multi-resolution bases.

B. Translation in the Wavelet Domain

During the translation stage at level v , the outgoing/incoming rays $\mathbf{G}_{l,\alpha}^\pm(\hat{\mathbf{k}}_q^v, t)$ are represented using their LCB coefficient vectors $\bar{\mathbf{I}}_\psi^\pm(\hat{\mathbf{k}}_q^v)$ in a single-resolution bases with $M' = M^{\min}$. Consider a far-field box pair composed of boxes α (source) and α' (observer). The coefficient vector of the incoming ray $\bar{\mathbf{I}}_\psi^-(\hat{\mathbf{k}}_q^v)$ (of length $N_I^- = M^{\min} N^-$) in α' can be computed by translating that of the outgoing ray $\bar{\mathbf{I}}_\psi^+(\hat{\mathbf{k}}_q^v)$ (of length $N_I^+ = M^{\min} N^+$) in α as

$$\bar{\mathbf{I}}_\psi^-(\hat{\mathbf{k}}_q^v) = \bar{\mathbf{T}} \bar{\mathbf{I}}_\psi^+(\hat{\mathbf{k}}_q^v) \quad (22)$$

where the translation matrix $\bar{\mathbf{T}}$ consists of matrix blocks $\bar{\mathbf{T}}_{sr}$, $s = 1, \dots, N^-$, $r = 1, \dots, N^+$ of dimension $M^{\min} \times M^{\min}$. The entries of these matrix blocks $\bar{\mathbf{T}}_{sr}$ [23]

$$\begin{aligned} \{\bar{\mathbf{T}}_{sr}\}_{wu} &= \langle T_{sw}^-(t), \mathcal{T}(\hat{\mathbf{k}}_q^v, t)^* T_{ru}^+(t) \rangle \\ &= \frac{1}{4\pi M^{\min} \Delta t} \int_{-\infty}^{+\infty} d\omega [\bar{B}_1^+(\omega - \omega_u) + \bar{B}_1^-(\omega - \omega_u)] \\ &\quad \times [\bar{B}_1^-(\omega - \omega_w) + \bar{B}_1^+(\omega - \omega_w)] e^{j\omega(a_s^+ - a_r^+)} \bar{\mathcal{T}}(\hat{\mathbf{k}}_q^v, \omega). \end{aligned} \quad (23)$$

Here, $T_{ru}^+(t)$ and $T_{sw}^-(t)$, $u, w = 1, \dots, M^{\min}$ are the LCB functions associated with intervals starting with a_r^+ and a_s^- , respectively, $\bar{B}_1^\pm(\omega)$ are the Fourier transformed bell functions associated with the first intervals of the outgoing/incoming ray, and $\bar{\mathcal{T}}(\hat{\mathbf{k}}_q^v, \omega)$ is the Fourier transform of the translation function $\mathcal{T}(\hat{\mathbf{k}}_q^v, t)$ [18]. Note that $\bar{\mathbf{T}}_{sr} = \bar{\mathbf{T}}_{(s-r+1)L}$ if $s \geq r$ and $\bar{\mathbf{T}}_{sr} = \bar{\mathbf{0}}$ if $s < r$. Hence, only matrix blocks $\bar{\mathbf{T}}_{s1}$, $s = 1, \dots, N^-$

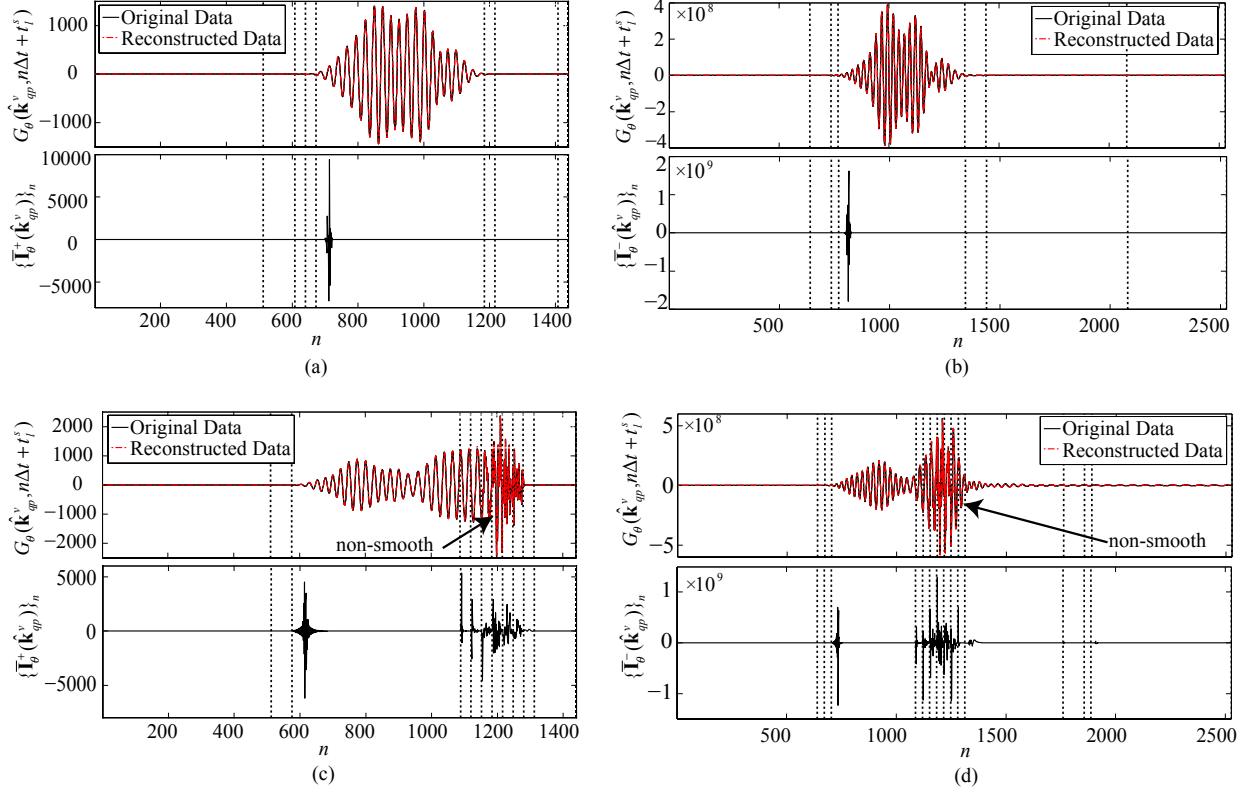


Fig. 4 LCB representation of one ray (θ component) in direction $\hat{\mathbf{k}}_{qp}^v = -\hat{\mathbf{x}}$ of a box of radius $R^v = 14\lambda$. (a) Outgoing ray, $\hat{\mathbf{k}} = \hat{\mathbf{z}}$. (b) Incoming ray, $\hat{\mathbf{k}} = \hat{\mathbf{z}}$. (c) Outgoing ray, $\hat{\mathbf{k}} = \hat{\mathbf{x}}$. (d) Incoming ray, $\hat{\mathbf{k}} = \hat{\mathbf{x}}$.

need to be computed. The computation of these block entries can be further facilitated by the following two observations: (i) $\{\bar{\mathbf{T}}_{sr}\}_{wu} = 0$ if $|u-w|$ is large, due to the narrow band nature of the LCB functions; (ii) when u is large, the translated LCB functions become temporally localized (see Appendix):

$$\begin{aligned} \mathcal{T}(\hat{\mathbf{k}}_{qp}^v, t)^* T_{ru}^+(t) &\approx \frac{c_0}{R_{c,\alpha\alpha'}} T_{ru}^+(t - R_{c,\alpha\alpha'}/c_0) f_1(\cos\theta) \\ &\quad - \frac{c_0}{R_{c,\alpha\alpha'}} T_{ru}^+(t + R_{c,\alpha\alpha'}/c_0) f_2(\cos\theta) \end{aligned} \quad (24)$$

where $f_1(\cos\theta) = \sum_{k=0}^{K^v} (-1)^k (2k+1) \Phi_k(\cos\theta)$ and $f_2(\cos\theta) = \sum_{k=0}^{K^v} (2k+1) \Phi_k(\cos\theta)$, i.e., the translated LCB function is locally supported on the interval $[a_r^+ - \varepsilon \pm R_{c,\alpha\alpha'}/c_0, a_{r+1}^+ + \varepsilon \pm R_{c,\alpha\alpha'}/c_0]$. Therefore, the non-trivial entries in the matrix blocks can be efficiently identified and computed. For example, one translation matrix is plotted in Fig. 2(a). Note that the translation matrices $\bar{\mathbf{T}}$ depend on the direction $\hat{\mathbf{k}}_{qp}^v$ and the vector $\mathbf{R}_{c,\alpha\alpha'}$ connecting the box centers, hence can be reused for group pairs with identical $\mathbf{R}_{c,\alpha\alpha'}$. When the translation stage at level- v is complete, the incoming ray data is converted to and stored in multi-resolution format.

C. Spherical Interpolation/Filtering in the Wavelet Domain

The outgoing/incoming rays in level $v > 1$ boxes are constructed/projected by spherical interpolation/filtering. [Note that those in $v=1$ boxes are constructed/projected by (11)/(14) followed by/following the compression/reconstruction of the

ray data using (21).] In this subsection, only the spherical interpolation used to construct the outgoing rays in the wavelet domain is expounded, as the wavelet domain spherical filtering leading to projection of incoming rays can be carried out similarly.

Consider construction of outgoing rays $\mathbf{G}_{l',\alpha'}^+(\hat{\mathbf{k}}_{qp}^v, t)$, $q = 0, \dots, K^v$, $p = -K^v, \dots, K^v$ in level- v box α' from the outgoing rays $\mathbf{G}_{l,\alpha}^+(\hat{\mathbf{k}}_{qp}^{v-1}, t)$, $q = 0, \dots, K^{v-1}$, $p = -K^{v-1}, \dots, K^{v-1}$ in its child box α . Let $\bar{\mathbf{I}}_\psi^+(\hat{\mathbf{k}}_{qp}^v)$ and $\bar{\mathbf{I}}_\psi^+(\hat{\mathbf{k}}_{qp}^{v-1})$ denote the LCB coefficient vectors that represent $\mathbf{G}_{l',\alpha'}^+(\hat{\mathbf{k}}_{qp}^v, t)$ and $\mathbf{G}_{l,\alpha}^+(\hat{\mathbf{k}}_{qp}^{v-1}, t)$ using single-resolution bases, respectively.

First, the coefficient vectors $\bar{\mathbf{I}}_\theta^+(\hat{\mathbf{k}}_{qp}^v)$ and $\bar{\mathbf{I}}_\theta^+(\hat{\mathbf{k}}_{qp}^{v-1})$ whose entries make up the quantities $I_{ru}^\theta(\hat{\mathbf{k}}_{qp}^v)\hat{\theta} + I_{ru}^\theta(\hat{\mathbf{k}}_{qp}^{v-1})\hat{\theta}$ are obtained by directly applying the global vector spherical interpolation scheme [1] to the quantities $I_{ru}^\theta(\hat{\mathbf{k}}_{qp}^{v-1})\hat{\theta} + I_{ru}^\theta(\hat{\mathbf{k}}_{qp}^{v-1})\hat{\theta}$ obtained from $\bar{\mathbf{I}}_\theta^+(\hat{\mathbf{k}}_{qp}^{v-1})$ and $\bar{\mathbf{I}}_\theta^+(\hat{\mathbf{k}}_{qp}^v)$.

Next, the interpolated LCB coefficients are shifted from the center of box α to that of box α' . Note that, in the time domain, the outgoing ray $\mathbf{G}_{l',\alpha'}^+(\hat{\mathbf{k}}_{qp}^v, t)$ in box α' is obtained by shifting the interpolated outgoing ray $\mathbf{G}_{l,\alpha}^+(\hat{\mathbf{k}}_{qp}^v, t)$ in box α as

$$\begin{aligned} \mathbf{G}_{l',\alpha'}^+(\hat{\mathbf{k}}_{qp}^v, t) &= \mathcal{S}(\hat{\mathbf{k}}_{qp}^v, t)^* \mathbf{G}_{l,\alpha}^+(\hat{\mathbf{k}}_{qp}^v, t) \\ &= \mathbf{G}_{l,\alpha}^+(\hat{\mathbf{k}}_{qp}^v, t - \hat{\mathbf{k}}_{qp}^v \cdot \mathbf{R}_{c,\alpha\alpha'}) . \end{aligned} \quad (25)$$

In contrast, in the wavelet domain, the coefficient vector $\bar{\mathbf{I}}_\psi^+(\hat{\mathbf{k}}_{qp}^v)$ can be computed by

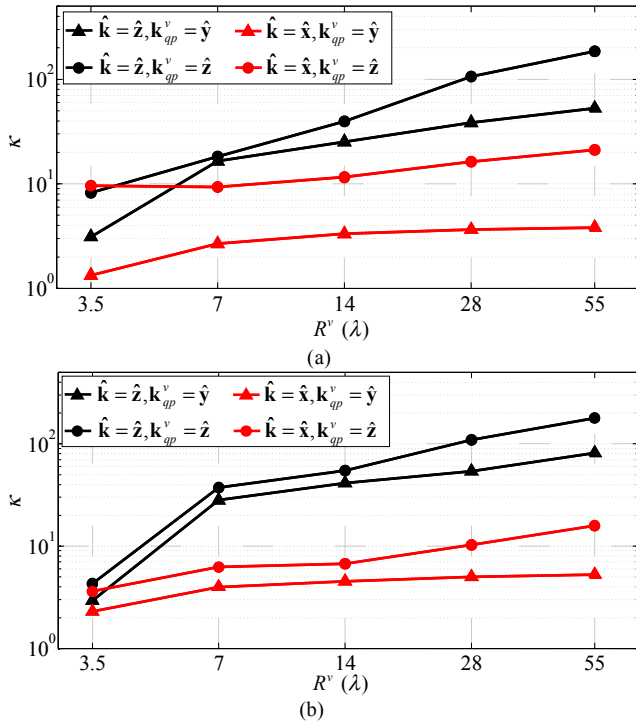


Fig. 5. Compression ratio κ of one ray in a box with radius R^v varying from 3.5λ to 55λ . (a) Outgoing ray. (b) Incoming ray.

$$\bar{\mathbf{I}}_{\psi}^{+'}(\hat{\mathbf{k}}_{qp}^v) = \bar{\bar{\mathbf{S}}} \bar{\mathbf{I}}_{\psi}^+(\hat{\mathbf{k}}_{qp}^v). \quad (26)$$

Here, $\bar{\bar{\mathbf{S}}}$ is a shifting matrix similar to the translation matrix $\bar{\bar{\mathbf{T}}}$. The entries of matrix block $\bar{\bar{\mathbf{S}}}_{sr}$, $r=1,...,N^+$, $s=1,...,N^{+}$ where N^{+} denotes the number of intervals in the support of $\mathbf{G}_{l,\alpha'}^+(\hat{\mathbf{k}}_{qp}^v, t)$,

$$\{\bar{\bar{\mathbf{S}}}_{sr}\}_{wu} = \left\langle T_{sw}^{+'}(t), \mathcal{S}(\hat{\mathbf{k}}_{qp}^v, t)^* T_{ru}^+(t) \right\rangle. \quad (27)$$

Here, $u, w = 1, ..., M^{\min}$, $T_{sw}^{+'}(t)$ are the LCB functions associated with the s^{th} interval in the support of $\mathbf{G}_{l,\alpha'}^+(\hat{\mathbf{k}}_{qp}^v, t)$. Just like the translation matrix, the shifting matrix is highly sparse [see the example in Fig. 2(b)] and can be reused for boxes α and α' that have the same $\mathbf{R}_{e,\alpha\alpha'}$. After the contributions from all child boxes have been accounted for, the LCB coefficient vector $\bar{\mathbf{I}}_{\psi}^{+'}(\hat{\mathbf{k}}_{qp}^v)$ of box α is converted to and stored in multi-resolution format.

D. Computational Complexity

In this section, the memory requirement and computational cost of the proposed LCB-enhanced PWT scheme are analyzed assuming S is smooth and quasi-planar, and illuminated by a plane wave. All estimates follow from the performance of the outgoing/incoming ray data compression using the LCBs. For a general structure, the ray data consists of locally smooth components that resemble the incident pulse, as well as the locally non-smooth components due to the APS function $T_{\text{APS}}(t)$ subdividing the temporal signature $f_n(t)$. These non-smooth components deteriorate the sparsity of the LCB

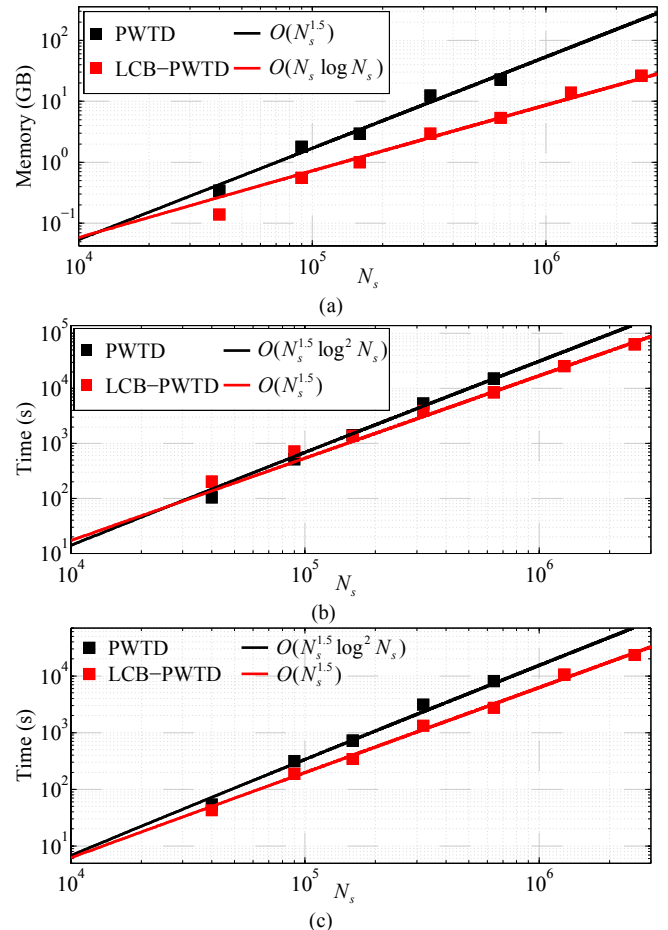


Fig. 6. (a) Memory cost of the ray data on one processor, and computation time of the (b) translation and (c) spherical interpolation/filtering stages of the PWT and LCB-PWT schemes. N_s increases from 40,000 to 2,560,000.

representation and degrade the overall performance of the scheme. However, for quasi-planar structures under certain types of excitations, current densities “propagate” along with the incident pulse, thereby generating sparsity in LCB representations of outgoing/incoming ray data that alleviate the abovementioned performance degradation and can help reduce the memory requirement and computational cost of the LCB-enhanced scheme. In what follows, the memory requirement and computational cost of the proposed LCB-enhanced PWT scheme are discussed.

The compression performance can be analyzed, without loss of generality, by an example (Fig. 3). In Fig. 3, a set of Hertzian dipoles, which are located at $\mathbf{r}_n = (x_n, y_n, z_n)$ and directed along $\hat{\mathbf{u}}_n$, are randomly sprinkled across a smooth quasi-planar surface S that is (approximately) parallel to the x - y plane. Here, $|z_n| \leq \varepsilon_z$ for some constant $\varepsilon_z \ll \lambda$. The temporal signature of the n^{th} dipole $f_n(t) = F(t - \mathbf{r}_n \cdot \hat{\mathbf{k}} / c_0)$. Here, $F(t)$ models an incidence pulse with temporal width t_{bw} , and $\hat{\mathbf{k}} = (\sin \theta^i, 0, -\cos \theta^i)$, where $\theta^i \leq 90^\circ$ is the direction of incidence. Let α be a level- v box centered at the origin with edge length $L^v = 2R^v / \sqrt{3}$. The outgoing ray $\mathbf{G}_{l,\alpha}^+(\hat{\mathbf{k}}_{qp}^v, t)$, where $\hat{\mathbf{k}}_{qp}^v = (\cos \phi_p^v \sin \theta_q^v, \sin \phi_p^v \sin \theta_q^v, \cos \theta_q^v)$, is constructed by

(11) with $\mathbf{S}_n(\mathbf{r}) = \hat{\mathbf{u}}_n \delta(\mathbf{r} - \mathbf{r}_n)$. It is assumed that each sub-signal $f_n^l(t)$ is possibly non-smooth near $t = lM^v\Delta t$ (or $t = (l-1)M^v\Delta t$) due to the presence of the APS function, which introduces non-smoothness in $\mathbf{G}_{l,\alpha}^+(\hat{\mathbf{k}}_{qp}^v, t)$ [Note that as the overall memory requirement and computational cost are dominated by those of higher levels of the PWT tree, this section assumes that box sizes are electrically large]. As the direction of incidence changes, the non-smoothness in sub-signals manifests itself differently for each dipole. In what follows, the memory and CPU complexities for two types of incidence are analyzed. Those for other incident angles can be estimated similarly.

1) Near-normal incidence

For excitations that are near-normal, the size of the computational domain along the direction of incidence $\hat{\mathbf{k}}$ (i.e., phase delay) is small. Each subsignal $f_n^l(t)$ therefore is almost identical and has vanishingly small non-smooth components. From (11), it is seen that rays for all directions have smooth temporal signatures that resemble the incident pulse (see Fig. 3(a)). As a result, the memory requirement for storing one outgoing/incoming ray in the proposed scheme scales essentially as $O(1)$, as opposed to $O(M^v)$ in the conventional PWT scheme.

As there exists ray data for N_k^v directions associated with N_g^v boxes, the overall memory requirements scale as $\sum_{v=1}^{N_L} N_g^v N_k^v O(1) = O(N_s \log N_s)$.

The computational cost of the translation stage is dominated by the wavelet-domain translation operation in (22). Although the translation matrix $\bar{\mathbf{T}}$ is highly sparse, its first few columns (corresponding to source LCB functions $T_{ru}^+(t)$ with small r) have $O(N_r^-) = O(M^v)$ nonzero entries; the remaining columns have $O(1)$ nonzero entries due to the localization property in (24). Since each LCB coefficient vector $\bar{\mathbf{I}}_\psi^+(\hat{\mathbf{k}}_{qp}^v)$ has $O(1)$ nonzero entries, the computational cost of each translation operation scales at most as $O(M^v)$. As there are $O(1)$ non-trivial outgoing rays at each direction in one source box, the overall computational cost of the translation stage scales as $\sum_{v=1}^{N_L} N_g^v N_k^v O(M^v) O(1) = O(N_s^{1.5})$.

The computational cost of the spherical interpolation stage is dominated by two operations: wavelet-domain spherical interpolation, and shifting. The spherical interpolation of one entry of the coefficient vectors $\bar{\mathbf{I}}_\psi^+(\hat{\mathbf{k}}_{qp}^{v-1})$ requires $O(N_k^v \log K^v)$ operations [20]; in contrast, shifting one entry of the interpolated coefficient vectors $\bar{\mathbf{I}}_\psi^+(\hat{\mathbf{k}}_{qp}^v)$ by (26) in all directions requires $O(N_k^v)$ operations as there are $O(1)$ non-zero entries in each column of the shifting matrix $\bar{\mathbf{S}}$. Since there are $O(1)$ non-trivial outgoing coefficients vectors, each having $O(1)$ nonzero entries for $O(N_g^v)$ source boxes, the computational complexity of the spherical interpolation stage scales as $\sum_{v=1}^{N_L} N_g^v O(1) O(1) O(N_k^v \log K^v) = O(N_s \log^2 N_s)$. Note that using a similar analysis, the computational cost of the spherical filtering stage is estimated as $\sum_{v=1}^{N_L} N_g^v O(N_t / M^v) O(1) O(N_k^v \log K^v) = O(N_s^{1.5})$. Here, it is assumed that there are $O(N_t / M^v)$ nontrivial incoming coef-

ficient vectors in each box as opposed to $O(1)$ outgoing ones due to resectioning of incoming rays with APS functions in the parent box.

2) Grazing incidence

Under grazing incidence (θ^i very small), the existence of non-smooth components of the ray data severely deteriorates the performance of the compression because certain subsignals, which contribute to the ray data, have non-smooth tails due to the presence of the APS function $T^{APS}(t)$.

Specifically, as illustrated in Fig. 3, a rectangular box of approximate dimensions $(c_0 t_{bw} / \sin \theta^i) \times L^v \times 2\mathcal{E}_z$ has dimension $c_0 t_{bw}$ along the direction of incidence. Therefore, dipoles confined to this box have subsignals with nontrivial non-smoothness. Note that solid blue lines represent non-smooth contributions in Fig. 3(b). From (11) and (14), the outgoing ray $\mathbf{G}_{l,\alpha}^+(\hat{\mathbf{k}}_{qp}^v, t)$ becomes locally non-smooth near time

$$\begin{aligned} t &= lM^v\Delta t + \hat{\mathbf{k}}_{qp}^v \cdot (\mathbf{r}_n - \mathbf{r}_s^c) / c_0 \\ &= lM^v\Delta t + (\cos \phi_p^v \sin \theta_q^v x_n + \sin \phi_p^v \sin \theta_q^v y_n + \cos \theta_q^v z_n) / c_0. \end{aligned} \quad (28)$$

The support of the non-smooth component of the outgoing ray therefore is at most $t_{bw} |\cos \phi_p^v \sin \theta_q^v| / \sin \theta^i + L^v |\sin \phi_p^v \sin \theta_q^v| / c_0 + 2\mathcal{E}_z |\cos \theta_q^v| / c_0$. When ϕ_p^v is small (i.e., the ray direction is close to the plane of incidence), the memory requirement to store one outgoing ray using LCBs essentially scales as $O(1)$ (see the example in Fig. 3). When ϕ_p^v is close to 90° (i.e., the ray direction is away from the plane of incidence), the memory requirement to store one outgoing ray using LCBs scales as $O(M^v)$ (see the example in Fig. 3). Note that similar analysis and results can be obtained for the incoming rays.

Because there is no asymptotic reduction in memory for ray data in directions ϕ_p^v near 90° , the memory requirement and computational cost of the LCB-enhanced PWT scheme asymptotically scale like those of the conventional PWT scheme. That said, in practice, memory requirement and computational cost of LCB-enhanced PWT scheme oftentimes are much lower than those of conventional PWT schemes as the asymptotic cost estimates have far smaller leading constants. Similarly, the solver has memory and CPU costs that are asymptotically identical to, though in practice much lower than, those of conventional PWT schemes when applied to general-structured scatterers.

IV. NUMERICAL RESULTS

This section presents numerical results that demonstrate the efficiency, accuracy, and applicability of the proposed LCB-enhanced PWT-TD-SIE solver. Unless stated otherwise, surfaces are illuminated by a plane wave with electric field

$$\mathbf{E}^i(\mathbf{r}, t) = \hat{\mathbf{p}} F(t - \mathbf{r} \cdot \hat{\mathbf{k}} / c_0). \quad (29)$$

Here, $F(t) = \cos[2\pi f_0(t - t_0)] e^{-(t-t_0)^2/2\sigma^2}$ is a modulated Gaussian, f_0 is the modulation frequency, $t_0 = 6\sigma$ is the delay

Table I: Memory requirements of the ray data and computational costs of the translation and spherical interpolation stages for the problem involving the NASA almond with $N_s = 507,156$ spatial basis functions

	Ray data (GB)	Translation (h)	Interpolation (h)
Reference	36.8	52.4	15.8
$\hat{\mathbf{k}} = \hat{\mathbf{x}}, \hat{\mathbf{p}} = \hat{\mathbf{z}}$	8.42	26.1	15.5
$\hat{\mathbf{k}} = \hat{\mathbf{x}}, \hat{\mathbf{p}} = \hat{\mathbf{y}}$	10.6	32.1	18.4
$\hat{\mathbf{k}} = \hat{\mathbf{z}}, \hat{\mathbf{p}} = \hat{\mathbf{y}}$	12.1	32.8	20.7

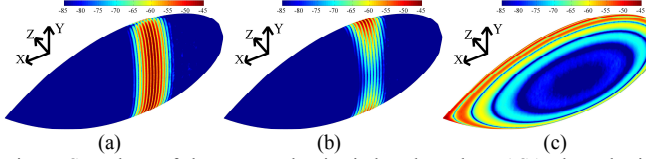


Fig. 7. Snapshots of the current density induced on the NASA almond with $N_s = 507,156$ spatial basis functions obtained by the LCB-enhanced PWT-D-TD-CFIE solver with (a) $\hat{\mathbf{k}} = \hat{\mathbf{x}}, \hat{\mathbf{p}} = \hat{\mathbf{z}}$ at $t = 520 \Delta t$, (b) $\hat{\mathbf{k}} = \hat{\mathbf{x}}, \hat{\mathbf{p}} = \hat{\mathbf{y}}$ at $t = 520 \Delta t$, (c) $\hat{\mathbf{k}} = \hat{\mathbf{z}}, \hat{\mathbf{p}} = \hat{\mathbf{y}}$ at $t = 600 \Delta t$

Table II: The technical data for the setups and solutions of scattering problems involving real-life targets

	NASA almond	Airbus A-320
Maximum dimension	0.25 m (185.26 λ)	37.5 m (123.46 λ)
Frequency (f_0, f_{bw})	(160, 60) GHz	(740, 245) MHz
Number of unknowns N_s	5,371,092	4,086,129
Time step size Δt	0.25 ps	50 ps
Number of time steps N_t	960	1,140
Number of processors	32	32
Memory (near field)	534 GB	775.7 GB
Memory (PWT-D)	1951 → 454 GB	601 → 158 GB
Setup time	3.2 h	8.9 h
RHS time (near field)	2 h	1.8 h
RHS time (PWT-D)	10.5 days	41 h
LHS time (GMRES)	4.6 h	51 min
RCS calculation time	18.8 h	16.7 h

imposed to ensure surface currents are vanishingly small for $t < 0$, $\sigma = 3/(2\pi f_{bw})$ is a measure of the pulse's duration, and $2f_{bw}$ represents the pulse's essential bandwidth; therefore maximum angular frequency $\omega_{max} = 2\pi(f_0 + f_{bw})$. Vectors $\hat{\mathbf{p}}$ and $\hat{\mathbf{k}}$ denote the polarization and propagation direction of the plane wave. All frequency domain (i.e., time harmonic) quantities presented in this section are obtained by normalizing the inverse Fourier transformed time-domain data by the spectrum

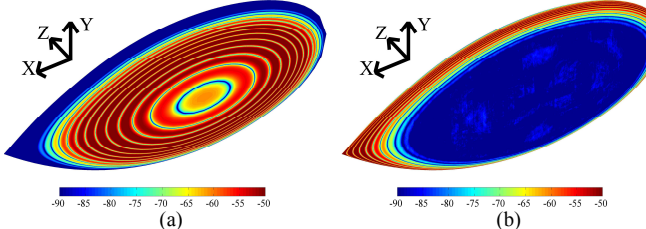


Fig. 9. Snapshots of the current density (in dB) induced on the NASA almond with $N_s = 5,371,092$ spatial basis functions obtained by the LCB-enhanced PWT-D-TD-CFIE solver at (a) $t = 300 \Delta t$, (b) $t = 440 \Delta t$, (c) $t = 460 \Delta t$, (d) $t = 560 \Delta t$

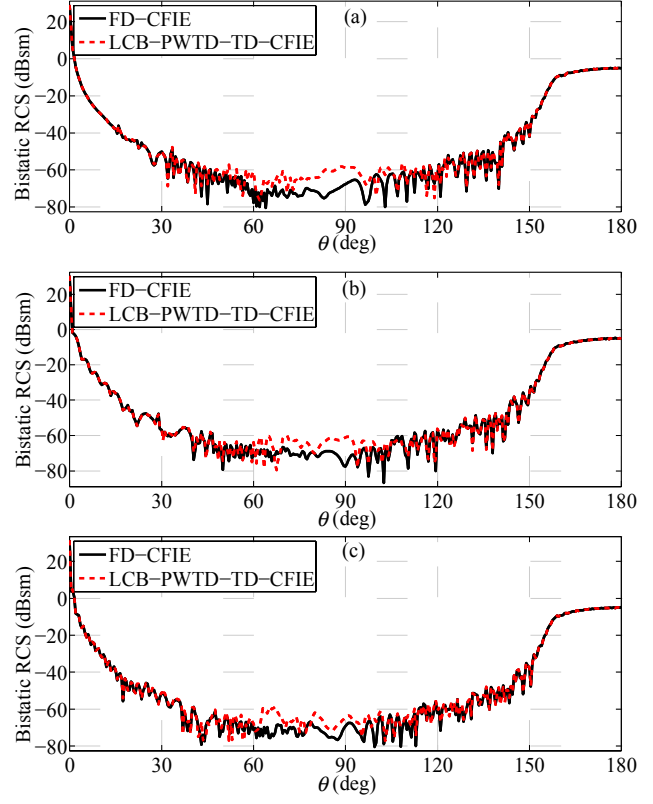


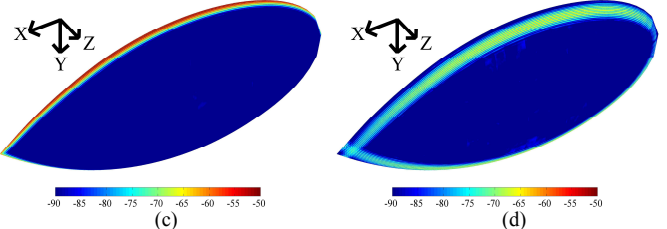
Fig. 8. Bistatic RCS of the NASA almond discretized with $N_s = 5,371,092$ spatial basis functions at (a) 140 GHz (b) 160 GHz and (c) 180 GHz computed at $\phi = 0^\circ$ and $\theta = [0, 180]^\circ$ by LCB-enhanced PWT-D-TD-CFIE solver and FD-CFIE solver.

of $F(t)$. A diagonally preconditioned generalized minimal residual (GMRES) scheme is used to iteratively solve (7) at each time step. The GMRES iteration is terminated when

$$\|\bar{\mathbf{V}}_j - \bar{\mathbf{Z}}_0 \bar{\mathbf{I}}_j^{(n)}\| < \delta \|\bar{\mathbf{V}}_j\| \quad (30)$$

with $\delta = 10^{-12}$ is reached. Here, $\bar{\mathbf{I}}_j^{(n)}$ represents the vector of current coefficients in the n^{th} iteration, and $\bar{\mathbf{V}}_j = \bar{\mathbf{F}}_j - \sum_{i=1}^{j-1} \bar{\mathbf{Z}}_i \bar{\mathbf{I}}_{j-i}$ is total RHS at time step j .

Simulations are performed on two computing platforms: (i) A Sandy Bridge compute-node with four eight-core 2.40 GHz Intel Xeon E5-4640 processors and 1 TB memory, and (ii) a Sandy Bridge cluster in which each node has two eight-core 2.60 GHz Intel Xeon E5-2670 processors and 64 GB memory.



The proposed solver uses the scalable PWTD parallelization scheme reported in [4, 24]. One MPI process is launched per compute-node and OpenMP processes exploit all cores on each node.

A. Compression of One Ray

First, the usefulness of LCBs in compressing outgoing/incoming rays is investigated. To this end, consider a far-field box pair with boxes labeled α and α' . Assume source box α encloses a square plate that resides in the x - y plane and is centered at the origin. A collection of randomly-oriented Hertzian dipoles are sprinkled across the plate. The temporal signature of the n^{th} dipole $f_n(t) = F(t - \mathbf{r}_n \cdot \hat{\mathbf{k}} / c_0)$ with $f_0 = 7.68$ GHz and $f_{bw} = 2.56$ GHz; the time step size is chosen as $\Delta t = 4.88$ ps. Outgoing rays are constructed using (11) with $\mathbf{S}_n(\mathbf{r}) = \hat{\mathbf{u}}_n \delta(\mathbf{r} - \mathbf{r}_n)$ and $\hat{\mathbf{u}}_n$ representing the orientation of the n^{th} dipole. Incoming rays are computed using the translation operation in (12). All ray data is compressed using a multi-resolution LCB with accuracy set to 1×10^{-3} . For simplicity, compression performance is only reported for the θ component of the ray data as performance for the φ component is very similar.

The entries of the coefficient vector $\{\bar{\mathbf{I}}_\theta^\pm(\hat{\mathbf{k}}_{qp}^v)\}_n$ and samples of the ray data $G_\theta(\hat{\mathbf{k}}_{qp}, n\Delta t + t_l^s)$, $n = 1, \dots, N_I^\pm$ obtained with $R^v = 14\lambda$ are plotted for $\hat{\mathbf{k}} = \hat{\mathbf{z}}$, $\hat{\mathbf{k}}_{qp}^v = -\hat{\mathbf{x}}$ in Figs. 4(a),(b) and for $\hat{\mathbf{k}} = \hat{\mathbf{x}}$, $\hat{\mathbf{k}}_{qp}^v = -\hat{\mathbf{x}}$ in Figs. 4(c),(d), respectively. Dashed vertical dashed lines correspond to ending points a_r^\pm , $r = 2, \dots, N^\pm$ of the intervals. When $\hat{\mathbf{k}} = \hat{\mathbf{z}}$, the dipole temporal signatures $F(t - \mathbf{r}_n \cdot \hat{\mathbf{k}} / c_0)$ resemble those of currents induced by normally incident plane waves, hence the outgoing/incoming rays are smooth (when the box is electrically large) and can be efficiently compressed by LCBs. In contrast, when $\hat{\mathbf{k}} = \hat{\mathbf{x}}$, the dipole temporal signatures resemble those of current densities induced by plane waves incident under grazing angles. In this case, outgoing and incoming rays possess locally non-smooth components that can be traced to the presence of APS functions. These non-smooth (and non-compressible) ray components however are easily identified by the LCBs [Fig. 4(c),(d)].

The compression ratio κ is defined as the length of the coefficient vector N_I^\pm divided by the number of its nontrivial entries. The compression ratios of outgoing and incoming rays with $\hat{\mathbf{k}} = \hat{\mathbf{z}}$, $\hat{\mathbf{k}}_{qp}^v = \hat{\mathbf{y}}$, $\hat{\mathbf{k}} = \hat{\mathbf{z}}$, $\hat{\mathbf{k}}_{qp}^v = \hat{\mathbf{z}}$, $\hat{\mathbf{k}} = \hat{\mathbf{x}}$, $\hat{\mathbf{k}}_{qp}^v = \hat{\mathbf{y}}$, and $\hat{\mathbf{k}} = \hat{\mathbf{x}}$, $\hat{\mathbf{k}}_{qp}^v = \hat{\mathbf{z}}$ obtained from boxes with different radii are plotted in Figs. 5(a)(b). For $\hat{\mathbf{k}} = \hat{\mathbf{z}}$, the compression ratio improves as the box size increases, which justifies our assumption about the $O(1)$ memory requirement to store one ray (in Section II-D). However, when $\hat{\mathbf{k}} = \hat{\mathbf{x}}$ (i.e., $\theta^v = 90^\circ$), the compression ratio in direction $\hat{\mathbf{k}}_{qp}^v = \hat{\mathbf{y}}$ (i.e., $\phi_p^v = 90^\circ$) remains constant as the box size increases. That said, significant memory savings are achieved when storing ray data using LCBs, irrespective of $\hat{\mathbf{k}}$.

B. Complexity Validation

Next, the memory requirement and computational complexity of the proposed LCB-enhanced PWTD scheme are validated.

Once again, a set of N_s Hertzian dipoles are randomly sprinkled across a square plate that resides in the x - y plane and is centered at the origin. The temporal signature of all dipoles is $f_n(t) = F(t)$ with $f_0 = 768$ MHz, and $f_{bw} = 256$ MHz, and the step size is $\Delta t = 62.5$ ps. The number of time steps is $N_t = 3.44N_s^{0.5}$. The ray data is compressed using LCBs with $M^{\min} = 16$ and accuracy set to 10^{-4} . Also, N_s is increased from 40,000 to 2,560,000 while the plate's edge length increases from 20λ to 160λ . The edge length of the smallest PWTD boxes is 1.25λ . The test is performed on cluster (ii) with 8 processors. The per-processor memory costs for the conventional and LCB-enhanced PWTD schemes are plotted in Fig. 6(a). Observed costs adhere to the $O(N_s^{1.5})$ and $O(N_s \log N_s)$ theoretical estimates. Irrespective of the choice of excitation, the LCB-enhanced PWTD scheme achieves significant memory savings compared to the conventional one. Computation times for the translation and spherical interpolation/filtering stages of the conventional and LCB-enhanced PWTD scheme are plotted in Figs. 6(b),(c); computation times for the LCB-enhanced scheme scale in good agreement with the theoretical predictions of $O(N_s^{1.5})$, as opposed to the $O(N_s^{1.5} \log^2 N_s)$ scaling exhibited by the conventional scheme.

C. NASA Almond

The proposed LCB-enhanced PWTD-TD-CFIE solver is applied to the analysis of transient scattering from a NASA almond that fits in a hypothetical box of dimensions $25\text{ cm} \times 9.7\text{ cm} \times 3.2\text{ cm}$. The almond is illuminated by $\mathbf{E}^i(\mathbf{r}, t)$ in (29) with $f_0 = 42$ GHz and $f_{bw} = 15$ GHz. Three different polarization-propagation direction configurations are considered: $\{\hat{\mathbf{k}} = \hat{\mathbf{x}}, \hat{\mathbf{p}} = \hat{\mathbf{z}}\}$, $\{\hat{\mathbf{k}} = \hat{\mathbf{x}}, \hat{\mathbf{p}} = \hat{\mathbf{y}}\}$, and $\{\hat{\mathbf{k}} = \hat{\mathbf{z}}, \hat{\mathbf{p}} = \hat{\mathbf{y}}\}$. The current density on the almond is discretized using $N_s = 507,156$ spatial basis functions. An eight-level PWTD tree is constructed upon setting the edge length of boxes at the finest level to 0.611λ and using $\gamma = 4$. The PWTD ray data is compressed using LCBs with $M^{\min} = 16$ and accuracy set to 10^{-3} . The simulation is carried out for $N_t = 1,300$ time steps with $\Delta t = 1$ ps on computing platform (i).

Snapshots of the current density on the almond computed during the simulations with different incident field configurations are plotted in Fig. 7. Table I presents the memory required to store the ray data and the computational costs of the PWTD translation and spherical interpolation stages. These costs are compared with those incurred by conventional PWTD-TD-CFIE solvers using incident field configuration with $\{\hat{\mathbf{k}} = \hat{\mathbf{x}}, \hat{\mathbf{p}} = \hat{\mathbf{z}}\}$. In this example, use of the LCB-enhanced PWTD scheme results in a 4.4-fold memory reduction and 1.5-fold speedup over the conventional scheme.

Next, the almond is illuminated by $\mathbf{E}^i(\mathbf{r}, t)$ in (29) with $f_0 = 160$ GHz, $f_{bw} = 60$ GHz, $\hat{\mathbf{p}} = \hat{\mathbf{y}}$, and $\hat{\mathbf{k}} = \hat{\mathbf{z}}$. The current density induced on the almond is discretized using $N_s = 5,371,092$ spatial basis functions. An eleven-level PWTD tree is constructed upon setting the edge length of boxes at the finest level to 0.488λ and using $\gamma = 4$. The PWTD ray data again is compressed using LCBs with $M^{\min} = 16$ and

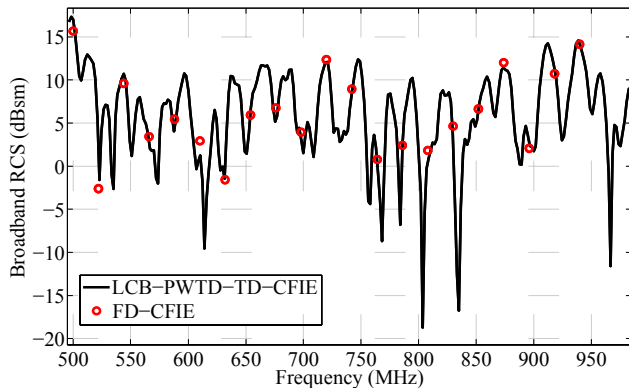


Fig. 10. Broadband RCS of the Airbus A-320 model along the $+z$ direction computed by LCB-enhanced PWTD-TD-CFIE solver and FD-CFIE solver.

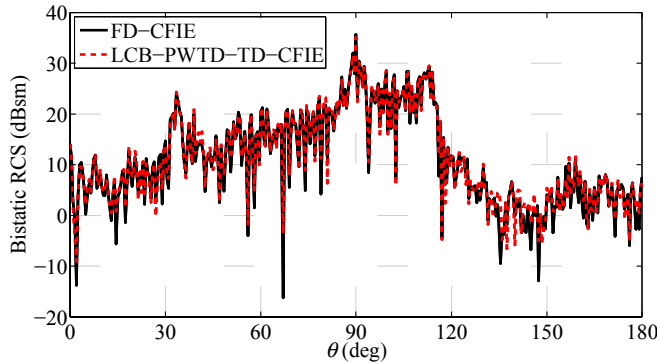


Fig. 11. Bistatic RCS of the Airbus A-320 model at 940 MHz computed at $\phi = 0^\circ$ and $\theta = [0, 180]^\circ$ by LCB-enhanced PWTD-TD-CFIE solver and FD-CFIE solver.

accuracy set to 10^{-3} . The simulation is carried out for $N_t = 960$ time steps with $\Delta t = 0.25$ ps on computing platform (ii).

Table II presents various parameters along with computational costs and memory requirements for the solver's different stages. The solver requires around 988 GB of memory and 11 days of CPU time when 32 processors are used. Note that the

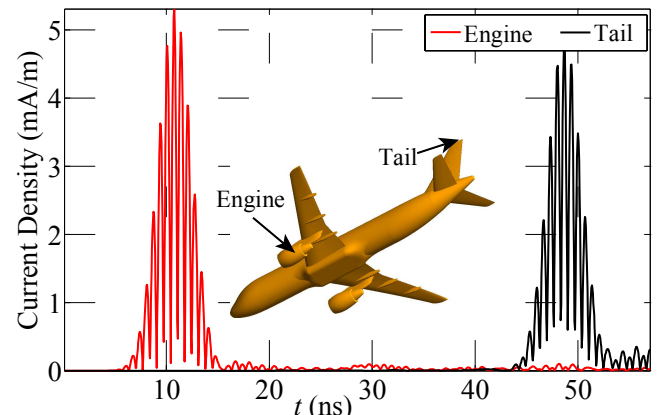


Fig. 12. Magnitudes of the current density at the engine intake and tail of the Airbus A-320 model computed by the LCB-enhanced PWTD-TD-CFIE solver.

memory requirement for the ray data is reduced from 1.95 TB to 454 GB by leveraging LCB-based compression. The bistatic RCS of the almond is computed at 140 GHz, 160 GHz, and 180 GHz, and compared to those obtained using a FD-CFIE solver in Fig. 8; results are in good agreement. In addition, snapshots of the current density induced on the almond at times $t = 300 \Delta t$, $440 \Delta t$, $460 \Delta t$, and $560 \Delta t$ reveal physical optics-like currents on the illuminated side of the almond and edge diffracted currents in the shadow region [Fig. 9].

D. Airplane Model

Finally, the LCB-enhanced PWTD-TD-CFIE solver is applied to the analysis of transient scattering from an Airbus-A320 model, which fits in a fictitious box with dimensions $34.2 \text{ m} \times 11.7 \text{ m} \times 37.5 \text{ m}$. The model airplane is illuminated by $\mathbf{E}^i(\mathbf{r}, t)$ in (29) with $f_0 = 740 \text{ MHz}$, $f_{bw} = 245 \text{ MHz}$, $\hat{\mathbf{p}} = \hat{\mathbf{z}}$, and $\hat{\mathbf{k}} = \hat{\mathbf{y}}$. The current density induced on the model airplane is discretized using $N_s = 4,086,129$ spatial basis functions. The PWTD ray data is represented using LCBs with $M^{\min} = 16$ and accuracy set to 10^{-3} . The simulation is carried out for $N_t = 1140$ time steps with $\Delta t = 50$ ps on computing

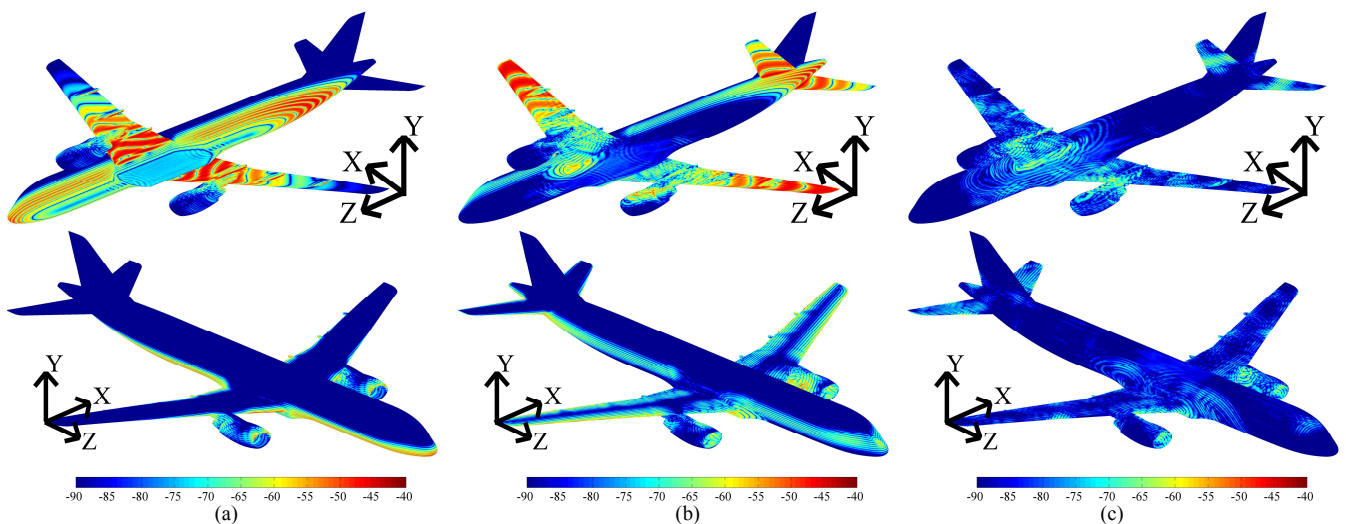


Fig. 13. Snapshots of the current density (in dB) induced on the Airbus A-320 model obtained by the LCB-enhanced PWTD-TD-CFIE solver at (a) $t = 380 \Delta t$, (b) $t = 480 \Delta t$, (c) $t = 640 \Delta t$

platform (ii). A ten-level PWT-D tree is constructed upon setting the side length of boxes at the finest level to 0.467λ and using $\gamma=4$.

Table II presents various parameters along with computational costs and memory requirements of the solver's different stages. The solver requires around 933.7 GB of memory and 69 hours of CPU time when 32 processors are used. Note that the memory requirement for the ray data is reduced from 601 GB to 158 GB by leveraging LCB-based compression. The broadband RCS of the airplane along the $+z$ direction ($\theta=0$) is computed using the LCB-enhanced PWT-D-TD-CFIE solver and an FD-CFIE solver; results obtained with both solvers presented in Fig. 10 are in good agreement. The bistatic RCS of the airplane is computed at 940 MHz and compared to the result obtained using the FD-CFIE solver in Fig. 11; again, results are in good agreement. Current densities induced at two points selected on the engine intake and the tail are computed and shown in Fig. 12. Finally, snapshots of the current induced on the model airplane at times $t = 380 \Delta t$, $480 \Delta t$, and $640 \Delta t$ are shown in Fig. 13.

V. CONCLUSION

This paper presents a local cosine wavelet-based compression scheme to reduce the memory requirement and computational cost of the multilevel PWT-D-accelerated MOT-based TD-SIE solver. The proposed scheme compresses the PWT-D ray data along the temporal dimension using LCBs and carries out the PWT-D operations including translation, shifting, and spherical interpolation/filtering in the wavelet domain. The resulting LCB-enhanced PWT-D-TD-SIE solver yields reduced memory and computational costs compared to the conventional PWT-D-TD-SIE solver. Indeed, when applied to the analysis of transient scattering from smooth quasi-planar objects under high frequency excitations with near-normal incidence angle, the memory requirement of the solver scales as $O(N_s \log N_s)$ and the computational cost scales as $O(N_s^{1.5})$. These scaling estimates are theoretically proved and validated by numerical examples. This LCB-enhanced PWT-D-TD-SIE solver is successfully applied to the analysis of transient scattering from canonical and real-life objects measuring well over one hundred wavelengths in size.

APPENDIX

To show the temporal localization property of the convolution of the LCB function with the translation function $\mathcal{T}(\hat{\mathbf{k}}_{qp}^v, t) * T_{ru}^+(t)$, we consider its Fourier transform $\bar{\mathcal{T}}(\hat{\mathbf{k}}_{qp}^v, \omega) \bar{T}_{ru}^+(\omega)$. The Fourier transform $\bar{\mathcal{T}}(\hat{\mathbf{k}}_{qp}^v, \omega) \bar{T}_{ru}^+(\omega)$ is:

$$\begin{aligned} \mathcal{T}(\hat{\mathbf{k}}_{qp}^v, \omega) \bar{T}_{ru}^+(\omega) &= 2i\omega \bar{T}_{ru}^+(\omega) \times \\ &\sum_{k=0}^{K^v} (-i)^k (2k+1) j_k(\omega R_{c,\alpha\alpha'} / c) \Phi_k(\cos \theta) \end{aligned} \quad (31)$$

where i is the imaginary unit and $j_k(\cdot)$ is the spherical Bessel function of order k . As discussed in Section III-A, the spec-

trum $\bar{T}_{ru}^+(\omega)$ of the LCB function has central frequency $\omega_u = \pi(u-1/2)/(M^r \Delta t)$ and bandwidth ω_{bw} . Here $\omega_{bw} \approx C\pi/(M^r \Delta t)$ for some constant C . In other words, $\bar{T}_{ru}^+(\omega) = 0$ if $\omega < \omega_u - \omega_{bw}$ or $\omega > \omega_u + \omega_{bw}$. When ω is sufficiently large (equivalently, u is large), the spherical Bessel function asymptotically behaves as

$$j_k(\omega R_{c,\alpha\alpha'} / c) \approx \frac{c \sin(\omega R_{c,\alpha\alpha'} / c - 1/2k\pi)}{\omega R_{c,\alpha\alpha'}}. \quad (32)$$

Substituting (32) into (31), $\bar{\mathcal{T}}(\hat{\mathbf{k}}_{qp}^v, \omega) \bar{T}_{ru}^+(\omega)$ can be re-written as

$$\begin{aligned} \bar{\mathcal{T}}(\hat{\mathbf{k}}_{qp}^v, \omega) \bar{T}_{ru}^+(\omega) &\approx \frac{c}{R_{c,\alpha\alpha'}} e^{i\omega R_{c,\alpha\alpha'} / c} \bar{T}_{ru}^+(\omega) f_1(\cos \theta) \\ &\quad - \frac{c}{R_{c,\alpha\alpha'}} e^{-i\omega R_{c,\alpha\alpha'} / c} \bar{T}_{ru}^+(\omega) f_2(\cos \theta) \end{aligned} \quad (33)$$

where $f_1(\cos \theta) = \sum_{k=0}^{K^v} (-1)^k (2k+1) \Phi_k(\cos \theta)$ and $f_2(\cos \theta) = \sum_{k=0}^{K^v} (2k+1) \Phi_k(\cos \theta)$. Upon inverse Fourier transform of (33), the convolution of the LCB function and the translation function, $\mathcal{T}(\hat{\mathbf{k}}_{qp}^v, t) * T_{ru}^+(t)$, can be expressed as

$$\begin{aligned} \mathcal{T}(\hat{\mathbf{k}}_{qp}^v, t) * T_{ru}^+(t) &\approx \frac{c}{R_{c,\alpha\alpha'}} T_{ru}^+(t - R_{c,\alpha\alpha'} / c) f_1(\cos \theta) \\ &\quad - \frac{c}{R_{c,\alpha\alpha'}} T_{ru}^+(t + R_{c,\alpha\alpha'} / c) f_2(\cos \theta). \end{aligned} \quad (34)$$

REFERENCES

- [1] B. Shanker, A. A. Ergin, M. Lu, and E. Michielssen, "Fast analysis of transient electromagnetic scattering phenomena using the multilevel plane wave time domain algorithm," *IEEE Trans. Antennas Propag.*, vol. 51, pp. 628-641, 2003.
- [2] B. Shanker, A. A. Ergin, and E. Michielssen, "Plane-wave-time-domain-enhanced marching-on-in-time scheme for analyzing scattering from homogeneous dielectric structures," *J. Opt. Soc. Am. A*, vol. 19, pp. 716-726, 2002.
- [3] J. Song, C.-C. Lu, and W. C. Chew, "Multilevel fast multipole algorithm for electromagnetic scattering by large complex objects," *IEEE Trans. Antennas Propag.*, vol. 45, pp. 1488-1493, 1997.
- [4] Y. Liu, A. C. Yuce, H. Bagci, and E. Michielssen, "A scalable parallel PWT-D-accelerated SIE solver for analyzing transient scattering from electrically large objects," *IEEE Trans. Antennas Propag.*, vol. 64, pp. 663-674, 2016.
- [5] G. Beylkin, R. Coifman, and V. Rokhlin, "Fast wavelet transforms and numerical algorithms I," *Comm. Pure Appl. Math.*, vol. 44, pp. 141-183, 1991.
- [6] R. L. Wagner and C. Weng Cho, "A study of wavelets for the solution of electromagnetic integral equations," *IEEE Trans. Antennas Propag.*, vol. 43, pp. 802-810, 1995.
- [7] W. L. Golik, "Wavelet packets for fast solution of electromagnetic integral equations," *IEEE Trans. Antennas Propag.*, vol. 46, pp. 618-624, 1998.

- [8] H. Deng and H. Ling, "Fast solution of electromagnetic integral equations using adaptive wavelet packet transform," *IEEE Trans. Antennas Propag.*, vol. 47, pp. 674-682, 1999.
- [9] G. W. Pan, Y. V. Tretiakov, and B. Gilbert, "Smooth local cosine based Galerkin method for scattering problems," *IEEE Trans. Antennas Propag.*, vol. 51, pp. 1177-1184, 2003.
- [10] Z. Zhou and J. S. Tyo, "An adaptive time-domain integral equation method for transient analysis of wire scatterer," *IEEE Antennas Wirel. Propag. Lett.*, vol. 4, pp. 147-150, 2005.
- [11] Y. Shifman and Y. Leviatan, "On the use of spatio-temporal wavelet expansions for transient analysis of wire antennas and scatterers," *IEEE Trans. Antennas Propag.*, vol. 52, pp. 2305-2318, 2004.
- [12] R. R. Coifman and Y. Meyer, "Remarques sur l'analyse de Fourier à fenêtre," *Comptes rendus de l'Académie des sciences. Série 1, Mathématique*, vol. 312, pp. 259-261, 1991.
- [13] C. Weng Cho, J. Jian-Ming, L. Cai-Cheng, E. Michielssen, and J. M. Song, "Fast solution methods in electromagnetics," *IEEE Trans. Antennas Propag.*, vol. 45, pp. 533-543, 1997.
- [14] B. Shanker, A. A. Ergin, K. Aygun, and E. Michielssen, "Analysis of transient electromagnetic scattering from closed surfaces using a combined field integral equation," *IEEE Trans. Antennas Propag.*, vol. 48, pp. 1064-1074, 2000.
- [15] Y. Shi, H. Bagci, and M. Lu, "On the internal resonant modes in marching-on-in-time solution of the time domain electric field integral equation," *IEEE Trans. Antennas Propag.*, vol. 61, pp. 4389-4392, 2013.
- [16] S. M. Rao, D. Wilton, and A. W. Glisson, "Electromagnetic scattering by surfaces of arbitrary shape," *IEEE Trans. Antennas Propag.*, vol. 30, pp. 409-418, 1982.
- [17] H. Bagci, A. E. Yilmaz, V. Lomakin, and E. Michielssen, "Fast solution of mixed-potential time-domain integral equations for half-space environments," *IEEE Trans. Geosci. Remote Sens.*, vol. 43, pp. 269-279, 2005.
- [18] A. A. Ergin, B. Shanker, and E. Michielssen, "The plane-wave time-domain algorithm for the fast analysis of transient wave phenomena," *IEEE Antennas Propag. Mag.*, vol. 41, pp. 39-52, 1999.
- [19] J. Knab, "Interpolation of band-limited functions using the approximate prolate series," *IEEE Trans. Inf. Theory*, vol. 25, pp. 717-720, 1979.
- [20] R. Jakob-Chien and B. K. Alpert, "A fast spherical filter with uniform resolution," *J. Comput. Phys.*, vol. 136, pp. 580-584, 1997.
- [21] M. V. Wickerhauser, *Adapted wavelet analysis from theory to software*: A K Peters/CRC Press, 1994.
- [22] K. Bittner and K. Gröchenig, "Direct and inverse approximation theorems for local trigonometric bases," *J. Approx. Theory*, vol. 117, pp. 74-102, 2002.
- [23] R.-S. Wu, Y. Wang, and M. Luo, "Beamlet migration using local cosine basis," *Geophysics*, vol. 73, pp. S207-S217, 2008.
- [24] Y. Liu, A. Al-Jarro, H. Bagci, and E. Michielssen, "Parallel PWTD-accelerated explicit solution of the time-domain electric field volume integral equation," *IEEE Trans. Antennas Propag.*, vol. 64, pp. 2378-2388, 2016.



Yang Liu (S'11-M'15) received the B.S. degree in electrical engineering from Shanghai Jiao Tong University, Shanghai, China, in 2010. He received the M.S. degrees in electrical engineering and mathematics from the University of Michigan, Ann Arbor, MI, USA, in 2013 and 2014, respectively. He received the Ph.D. degree in electrical engineering from the University of Michigan, Ann Arbor, MI, USA, in 2015.

Since August 2010, he has been a graduate Research Assistant at the Radiation Laboratory, University of Michigan. Since June 2015, he has been working as a Research Fellow at the Radiation Laboratory, University of Michigan. His main research interest is in computational electromagnetics, with focus on fast time domain and frequency domain integral equation methods.

Dr. Liu authored the second place paper of the student paper competition of the 28th International Review of Progress in Applied Computational Electromagnetics, 2012. He also co-authored the first place paper of the student paper competition of the 12th International Workshop on Finite Elements for Microwave Engineering, 2014.



Abdulkadir C. Yücel received the B.S. degree in electronics engineering (*Summa Cum Laude*) from Gebze Institute of Technology, Kocaeli, Turkey, in 2005, and the M.S. and Ph.D. degrees in electrical engineering from the University of Michigan, Ann Arbor, MI, USA, in 2008 and 2013, respectively.

From September 2005 to August 2006, he worked as a Research and Teaching Assistant at the Electronics Engineering Department, Gebze Institute of Technology. From August 2006 to May 2013, he was a Graduate Student Research Assistant at the Radiation Laboratory, University of Michigan. Since May 2013, he has been working as a Research Fellow at the Radiation Laboratory, University of Michigan.

Dr. Yücel received the Fulbright Fellowship in 2006 and Electrical Engineering and Computer Science Departmental Fellowship of University of Michigan in 2007. His research interests include various aspects of computational electromagnetics with emphasis on uncertainty quantification for electromagnetic analysis on complex platforms, electromagnetic compatibility and interference analysis, nature-based design of electromagnetic devices, and integral equation based frequency and time domain solvers and their accelerators.



Hakan Bağcı (S'98-M'07-SM'14) received the B.S. degree in electrical and electronics engineering from the Bilkent University, Ankara, Turkey, in June 2001 and the M.S. and Ph.D. degrees in electrical and computer engineering from the University of Illinois at Urbana-Champaign, IL, USA, in 2007 and 2014, respectively.

na-Champaign (UIUC), Urbana, IL, USA, in August 2003 and January 2007, respectively.

From June 1999 to July 2001, he worked as an Undergraduate Researcher at the Computational Electromagnetics Group, Bilkent University. From August 2001 to December 2006, he was a Research Assistant at the Center for Computational Electromagnetics and Electromagnetics Laboratory, UIUC. From January 2007 to August 2009, he worked as a Research Fellow at the Radiation Laboratory, University of Michigan. In August 2009, he joined the Division of Physical Sciences and Engineering at the King Abdullah University of Science and Technology (KAUST), Thuwal, Saudi Arabia, as an Assistant Professor of electrical engineering. His research interests include various aspects of computational electromagnetics with emphasis on time domain integral equations and their fast marching-on-in-time-based solutions, well-conditioned integral-equation formulations, and development of fast hybrid methods for analyzing statistical EMC/EMI phenomena on complex and fully loaded platforms.

Dr. Bağcı was the recipient of the 2008 International Union of Radio Scientists (URSI) Young Scientist Award and the 2004–2005 Interdisciplinary Graduate Fellowship from the Computational Science and Engineering Department, UIUC. His paper titled “Fast and Rigorous Analysis of EMC/EMI Phenomena on Electrically Large and Complex Structures Loaded With Coaxial Cables” was one of the three finalists (with honorable mention) for the 2008 Richard B. Schulz Best Transactions Paper Award given by the IEEE Electromagnetic Compatibility Society. He authored and coauthored three finalist papers and another paper, which is awarded honorable mention, in the student paper competitions at the 2005, 2008, and 2010 IEEE Antennas and Propagation Society International Symposiums.



Anna C. Gilbert (M'05) received an S.B. degree from the University of Chicago and a Ph.D. from Princeton University, both in mathematics. In 1997, she was a postdoctoral fellow at Yale University and AT&T Labs-Research. From 1998 to 2004, she was a member of technical staff at AT&T Labs-Research in Florham Park, NJ. Since then she has been with the Department of Mathematics at the University of Michigan, where she is now a Professor. She has received several awards, including a Sloan Research Fellowship (2006), an NSF CAREER award (2006), the National Academy of Sciences Award for Initiatives in Research (2008), the Association of Computing Machinery (ACM) Douglas Engelbart Best Paper award (2008), the EURASIP Signal Processing Best Paper award (2010), a National Academy of Sciences Kavli Fellow (2012), and the SIAM Ralph E. Kleinman Prize (2013).

Her research interests include analysis, probability, networking, and algorithms. She is especially interested in randomized algorithms with applications to harmonic analysis, signal and image processing, networking, and massive datasets.



Eric Michielssen (M'95–SM'99–F'02) received the M.S. degree in electrical engineering (*Summa Cum Laude*) from

the Katholieke Universiteit Leuven (KUL), Leuven, Belgium, in 1987, and the Ph.D. degree in electrical engineering from the University of Illinois at Urbana-Champaign (UIUC), Urbana, IL, USA, in 1992.

He joined the faculty of the UIUC Department of Electrical and Computer Engineering in 1993, reaching the rank of Full Professor in 2002. In 2005, he joined the University of Michigan (UM) as a Professor of Electrical Engineering and Computer Science. Since 2009, he has been directing the University of Michigan Computational Science Certificate Program. He authored or coauthored more than 160 journal papers and book chapters and more than 300 papers in conference proceedings. His research interests include all aspects of theoretical and applied computational electromagnetics. His research focuses on the development of fast frequency and time domain integral-equation-based techniques for analyzing electromagnetic phenomena, and the development of robust optimizers for the synthesis of electromagnetic/optical devices.

Dr. Michielssen received a Belgian American Educational Foundation Fellowship in 1988 and a Schlumberger Fellowship in 1990. Furthermore, he received a 1994 International Union of Radio Scientists (URSI) Young Scientist Fellowship, a 1995 National Science Foundation CAREER Award, and the 1998 Applied Computational Electromagnetics Society (ACES) Valued Service Award. In addition, he was named 1999 URSI United States National Committee Henry G. Booker Fellow and selected as the recipient of the 1999 URSI Koga Gold Medal. He also was awarded the UIUC's 2001 Xerox Award for Faculty Research, appointed 2002 Beckman Fellow in the UIUC Center for Advanced Studies, named 2003 Scholar in the Tel Aviv University Sackler Center for Advanced Studies, selected as UIUC 2003 University and Sony Scholar; in 2011 he received the UM College of Engineering David E. Liddle Research Excellence Award. He is a member of URSI Commission B. He served as the Technical Chairman of the 1997 Applied Computational Electromagnetics Society (ACES) Symposium (Review of Progress in Applied Computational Electromagnetics, March 1997, Monterey, CA, USA), and served on the ACES Board of Directors (1998–2001 and 2002–2003) and as ACES Vice-President (1998–2001). From 1997 to 1999, he was an Associate Editor for Radio Science, and from 1998 to 2008 he served as an Associate Editor for the IEEE TRANSACTIONS ON ANTENNAS AND PROPAGATION.